MICHIGAN STATE UNIVERSITY

CYCLOTRON LABORATORY

FISSION FOLLOWING CAPTURE REACTIONS OF $^{32}S + ^{208}Pb$

M.B. TSANG, D. ARDOUIN, C.K. GELBKE, W.G. LYNCH,
Z.R. XU, B.B. BACK, R. BETTS, S. SAINI, P.A. BAISDEN
and M.A. McMAHAN

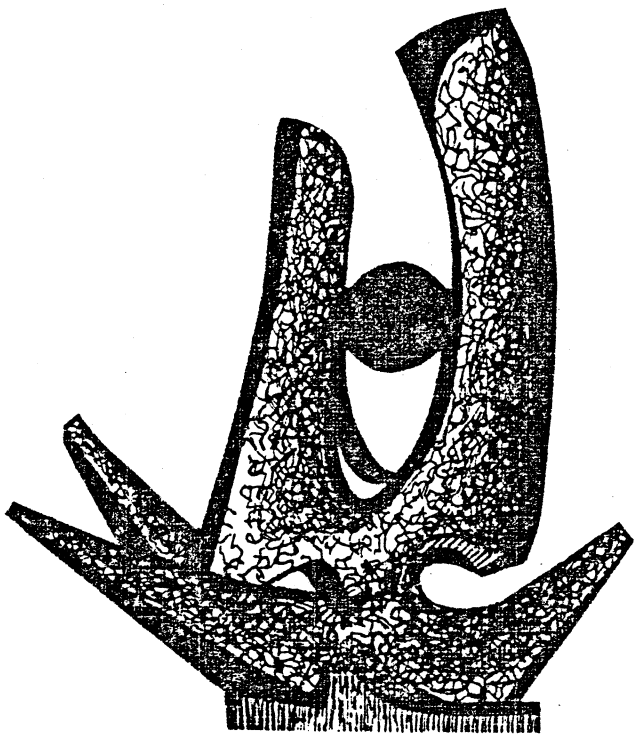

FEBRUARY 1983

MSUCL-396

MSUCL-399
February 1983

FISSION FOLLOWING CAPTURE REACTIONS OF $^{32}S + ^{208}Pb$

M.B. Tsang, D. Ardouin*, C.K. Gelbke, W.G. Lynch, and Z.R. Xu
National Superconducting Cyclotron Laboratory
Michigan State University
East Lansing, MI 48824

B.B. Back, R. Betts, and S. Saini
Chemistry Division, Argonne National Laboratory
Argonne, IL 60439

P.A. Baisden and M.A. McMahan
Nuclear Chemistry Division, Lawrence Livermore National
Laboratory, Livermore, CA 94550

PACS Number: 25.70.Jj

Abstract

Fission fragment mass and angular distributions were measured for ^{32}S induced reactions on ^{208}Pb at the laboratory energies of 180, 210, 250, and 266 MeV. By measuring the folding angle distributions between coincident fission-like fragments at several beam energies it is shown that essentially the entire mass of the projectile is transferred to the composite system which subsequently decays via symmetric fission. With increasing projectile energy the width of the mass distribution increases approximately as the square root of the nuclear temperature. The energy dependence of the angle integrated fusion-fission cross sections can be well described by classical trajectory calculations using the proximity potential and one-body dissipation. The fission fragment angular distributions become more anisotropic with increasing beam energy. Even at the lowest energy of 180 MeV, the angular distributions are more anisotropic than expected from statistical model calculations using saddle point shapes of the rotating liquid drop model. A simple parameterization of the angular momentum dependence of the effective moment of inertia gives a consistent description of the energy dependence of the angular distributions.

Introduction

The concept of compound nucleus formation and decay is expected to become meaningless for angular momenta exceeding the value $\ell_{Bf=o}$ for which the fission barrier vanishes. It has been known for several years[1-3] that the cross sections for fusion-fission-like processes may considerably exceed the sharp cut-off limit for compound nucleus formation, $\sigma_{CN}^{max} = \pi\lambda^2 \ell_{Bf=o}^2$, as calculated from the rotating liquid drop model.[4] It has been suggested[5-8] that a new reaction mechanism, "fast fission", should set in for partial waves greater than $\ell_{Bf=o}$ but less than ℓ_{cr}, where ℓ_{cr} is the maximum angular momentum for which the entrance channel potential exhibits a pocket and for which capture of the projectile by the target nucleus occurs. The interaction time for fast fission is expected to involve time scales intermediate between compound nucleus formation and statistical decay on the one extreme and deeply inelastic scattering on the other.

The occurrence of fast fission processes has also been suggested in the context of more general considerations on the dynamics of fusion of two nuclei[9-11]. For the dynamical evolution of nucleus-nucleus collisions three configurations and, correspondingly, three energy thresholds have been pointed out to be of special importance: (i) the contact configuration for which neck formation becomes energetically favorable, (ii) the conditional saddle point configuration corresponding to the saddle point in a multidimensional potential energy surface for fixed mass asymmetry, and (iii) the fission saddle point configuration. Nuclear collisions leading to a contact configuration which is outside the

conditional saddle point correspond to dinuclear deeply inelastic reactions, whereas compound nucleus formation requires a configuration inside the fission saddle point (assuming the existence of a non-vanishing fission barrier). Reactions, on the other hand, that overcome the conditional saddle point but the not fission saddle point correspond to fast fission (mono-nucleus) reactions.

Although the occurrence of fast fission appears to be well justified theoretically, the experimental signatures of this process are less well established. For interaction times shorter than the rotational period of the corresponding mononucleus, the angular distributions of non-symmeteric fragments will no longer be symmetric about 90^{o} in the center-of-mass system. This signature provides clear proof for a reaction not involving compound nucleus formation. Up to now, such angular asymmetries have been observed[12] primarily for heavier projectiles ($A \gtrsim 50$) for which the distinction between deeply inelastic reactions and fast fission is less clear.

It has also been proposed that fast fission processes should exhibit broader mass distributions than conventional compound nucleus fission[5-8]. A first survey[5] of the angular momentum dependence of fission fragment mass distributions provided evidence for an abrupt increase of the widths of fission fragment mass distributions once the entrance channel angular momenta exceed the value $\ell_{Bf=o}$. However, this effect appears to be less pronounced in more recent investigations[8,13]. In terms of the angular momentum dependence of the widths

of the mass distributions, the distinction between compound nucleus fission and fast fission is complicated by the fact that the stiffness parameter for the mass asymmetry degree of freedom of the potential energy surface is expected to decrease[14] for higher angular momenta. As a consequence, the widths of fission fragment mass distributions are expected to increase more rapidly with increasing beam energy than expected from the pure temperature dependence, $\Delta M \sim T^{\frac{1}{2}}$, an effect which has not yet been accounted for in a quantitative way.

For the case of compound nucleus fission, fission fragment angular distributions provide information about the shape of the saddle point configuration[15]. At sufficiently high excitation energies, the saddle point configurations derived from angular distribution measurements were found to be in agreement with the liquid drop model. Recent investigations[16-19] of fission fragment angular distributions measured for ^{32}S induced reactions on heavy targets have revealed unexpectedly larger angular anisotropies, in clear contrast to predictions from the rotating liquid drop model. It has been suggested[17,18] that these large angular anisotropies should present a sensitive indication for the occurrence of fast fission processes.

In order to further elucidate the possible experimental signatures of fast fission reactions, we have studied fission processes following the capture of ^{32}S projectiles by ^{208}Pb target nuclei over the incident energy range of 180-270 MeV. At the lower end of this energy range, the reaction

is expected to proceed via compound nucleus formation followed by the subsequent statistical fission decay. At the higher energies, on the other hand, the entrance channel angular momenta leading to the capture of target and projectile considerably exceed the value $\ell_{Bf=o}$ and fast fission is expected to occur. Based on the foregoing arguments, we measured energy and mass distributions with good statistical accuracy at 180, 210, 250, and 266 MeV incident energies. In an earlier experiment, distributions of the folding angle between two coincident fission fragments were measured.

Details of the experimental set up and the data analysis will be given in Section II and in Appendix I, respectively. The results of the folding angle distribution measurements will be discussed in Section III. In Section IV, fission fragment mass distributions will be presented. The energy dependence of the integrated cross sections and the angular distributions will be discussed in Sections V and VI, respectively. Details about the ambiguities arising for the interpretation of the angular distributions at low energies will be given in Appendix II. A summary will be given in Section VII.

II. Experimental Set-Up

The experiments were performed at the Argonne National Laboratory Superconducting Linear Accelerator using a pulsed ^{32}S beam of a 20.6 ns repetition rate. Depending on beam energy, time resolutions were typically between 200 and 500 ps. For the experiment, a ^{208}Pb target of 200 $\mu g/cm^2$ areal density was used.

The detector arrangement in the scattering chamber is shown in Figure 1. For all detectors, time-of-flight measurements were performed by recording the detector time response relative to the phase of the accelerator radio frequency. Two solid state detectors mounted out-of-plane at the fixed laboratory scattering angles of $+24^{\circ}$ and -21° were used to monitor the cross section normalization and the time calibration with respect to the RF phase. At forward angles, fission fragments were detected with a solid state ΔE-E detector telescope consisting of a 5 μm ΔE-and a 150 μm E-surface barrier detectors. This telescope was located at a distance of 30 cm from the target and subtended a solid angle of 0.26 msr. At backward angles, fission fragments were detected by a 30 μm surface barrier detector backed by a 100 μm thick veto detector used to identify and reject light particles. This telescope was placed at a distance of 18 cm from the target and subtended a solid angle of 0.98 msr.

Fission fragment folding angle distributions were measured by detecting coincident fission fragments with a position sensitive solid state detector (PSD) and a surface barrier detector used for energy and time-of-flight measurements. The position sensitive detector was placed at a distance of 9 cm from the target and subtended an angular range of 30° in the reaction plane. The time-of-flight detector was mounted at a distance of 39 cm from the target and subtended a solid angle of 1.6 msr. For the measurement of the folding angle distributions, the center of the PSD was moved from -70° to -90° while the angle of the time-of-flight

detector was moved from 60^{o} to 85^{o}. The absolute accuracy of the folding angle distribution measurements was limited to about $\Delta\theta_{AB} \approx 2^{o}$ due to the close geometry of the position sensitive detector and the large aperture (ϕ = 3mm) of the beam collimator that was placed at the entrance of the scattering chamber.

For the measurement of fission fragment mass distributions a channel plate was placed in front of the surface barrier detector at a distance of 15.4 cm from the target, and the position sensitive detector was replaced by a 600 mm^2 surface barrier detector of 0.2 sr solid angle. This detector was positioned at the maximum of the folding angle distribution and was used to detect coincident fission fragments. In order to avoid the uncertainties of the mass dependent plasma delay[20] for silicon detectors the channel plate was used for the velocity measurements while the silicon detector was used for the energy measurements and to resolve the time-of-flight ambiguities that arise from RF timing at high beam pulse repetition rates. The energy calibration of the silicon detectors was established by using the procedure of ref. 21.

In order to establish the absolute cross section normalization, the elastic Rutherford scattering was measured at forward angles using the ΔE-E telescope and the two monitor detectors. The absolute normalization of the backward angle telescope was obtained from the known geometry. The relative normalization of the cross sections was established by measuring the elastic scattering in the two monitor detectors and by measuring the integrated beam current. The absolute

normalization of the cross section calibration is believed to be accurate to better than 10% and the relative cross section uncertainties are given by the error bars in the appropriate figures.

For all detectors the energy signals and the time signals relative to the phase of the accelerator radio frequency were written on magnetic tape and analyzed off-line. Some details concerning corrections for neutron evaporation and kinematic transformations into the center-of-mass system are given in Appendix I.

III. Folding Angle Distributions

From the measurement of the folding angle between two coincident fission fragments, information about the linear momentum of the fissioning nucleus can be obtained[22-25]. With increasing recoil velocity of the parent nucleus, the two fission fragments are emitted to more forward angles, i.e. decreasing folding angles between two coincident fission fragments correspond to larger linear momenta of the parent nucleus. By means of this technique, fusion-like reactions can be readily distinguished from quasi-elastic or deeply inelastic reactions[23].

Figure 2 shows the variation of the most probable folding angle with projectile energy. The dashed lines correspond to folding angles calculated for symmetric fission of the composite system assuming linear momentum transfers of 80, 90, and 100% of the beam momentum. For these calculations, the total kinetic energy release of TKE=188 MeV has been taken from the systematics of ref. 26. As can be seen from the figure, more than 90% of the projectile momentum is

transferred to the parent nucleus prior to fission. Within the accuracy of the experiment, the data are consistent with fission following capture.

In Figure 3 we show a scatter plot of folding angle vs. fragment mass for the incident energy of 270 MeV. The folding angle distribution was found to be asymmetric with a tail which extends toward smaller folding angles for more asymmetric mass divisions. This asymmetry is of purely kinematic origin as is shown by the solid line which corresponds to compound nucleus fission assuming a total kinetic energy of 188 MeV.

At higher beam energies, $E_{lab} \gtrsim 250$ MeV, there is evidence of sequential fission following deeply inelastic reactions. Except at backward angles, this process could be clearly separated from fission following capture. As an example, Figure 4 shows a contour plot of energy vs. fragment mass measured at E_{lab}=266 MeV and θ_{lab}=40°. Two groups of heavy fragments can be distinguished, consistent with fission following capture reactions and fission following deeply inelastic reactions. Even at the highest energy investigated deeply inelastic processes contribute only about 8% to the total fission cross section. Possible contributions of fission following deeply inelastic reactions to the capture cross sections are estimated to be smaller than our experimental uncertainties.

IV. Mass Distributions

The masses of secondary fission fragments after neutron evaporation are determined from the measurements of energy and velocity. In order to deduce the mass distributions of the primary fragments we have corrected for the effects of neutron evaporation and possible kinematic distortions as described in more detail in Appendix I.

Over the range of beam energies investigated the kinematic distortions of the mass spectra are small. However, the effects from neutron evaporation are appreciable, as is demonstrated in Figure 5. The upper part of the figure shows the average values (solid curves) and variances (vertical bars) of the estimated number of neutrons emitted by a given primary fragment. The variances shown in the figure reflect the variations of the total kinetic energy for fixed fragment mass and do not include the additional broadening arising from temperature fluctuation or from the statistical nature of the neutron emission process. The measured laboratory distributions of secondary fragments (triangles) and the extracted primary mass distributions in the center-of-mass system (circles) are given in the lower part of the figure. The main effects of the neutron evaporation correction are to shift the centroid of the mass distribution towards A=120, corresponding to symmetric mass division, and to increase the width of the primary mass distribution. With increasing beam energy, the neutron evaporation becomes more important as can be seen by comparing the mass distributions at 180 and 266 MeV.

Within the accuracy of our measurements, the centroids

and widths of the mass distributions were found to be independent of scattering angle. This result is in qualitative agreement with the results of ref. 12 where significant angular variations of the mass distributions were detected for reactions induced by ^{208}Pb projectiles on targets heavier than ^{48}Ca but not on a ^{26}Mg target. The angular independence of the measured mass distributions is consistent with interaction times that are larger than the characteristic time to reach equilibration of the mass symmetry degree of freedom.

In order to obtain mass spectra with better statistical accuracy the data taken at different angles were added. The resulting mass distributions are symmetric about A≈120 and become broader with increasing beam energy; see Figure 6. In Figure 7, the widths of the mass distributions, ΔM_{FWHM}, are plotted *vs.* ℓ_c, the sharp cut-off angular momentum for capture. The value of ℓ_c is determined from the angle integrated fission cross sections, σ_f, using the relation

$$\sigma_f = \pi\lambda^2(\ell_c+1)^2. \qquad (1)$$

We do not find positive evidence for a sudden increase of ΔM_{FWHM} for $\ell_c > \ell_{Bf=o}\approx 60\,\hbar$. However, the number of data points and the accuracy of the present measurements cannot rule out a small discontinuity in the rate of increase of ΔM_{FWHM} in the vicinity of $\ell_c \approx \ell_{Bf=o}$.

The widths of fission fragment mass distributions are expected to increase both for larger angular momenta and for higher temperatures of the composite nucleus. With increasing angular momentum the stiffness parameter of the potential energy associated with the mass asymmetry degree

of freedom at the saddle point is expected to decrease[14]. As a consequence, the mass distributions should become wider. Since this effect has not yet been accounted for in a quantitative manner, we make the simplifying assumption that the stiffness parameter is independent of angular momentum. If statistical equilibrium and a harmonic potential for the mass asymmetry degree of freedom are assumed, the width of the mass distribution is proportional to the square root of the temperature T at the saddle point,

$$\Delta M_{FWHM} = \text{Const} \cdot T^{\frac{1}{2}}. \qquad (2)$$

In order to evaluate the temperature, we have used the relation

$$T^2 = \frac{8.5\ \text{MeV}}{A}\,(E^* - \langle E_{rot}\rangle). \qquad (3)$$

where A, E^*, and $\langle E_{rot}\rangle$ are the mass number, the excitation energy, and the average energy of collective rotation, respectively. We assume that no energy is removed from the composite system by prefission light particle emission. The average rotational energy is calculated by using the moment of inertia of a rigidly rotating sphere $\mathcal{J}_o = 133\ \hbar^2\ \text{MeV}^{-1}$. This procedure leads to an overestimate of the average rotational energy and, correspondingly, to an underestimate of the temperature.

The temperature dependence of ΔM_{FWHM} calculated from eqs. 2 and 3 is shown by the dot-dashed curve in Figure 7. For comparison, the dashed curve shows the expected temperature dependence if the rotational energy is neglected. For these calculations, the proportional constant in eq. 2 was normalized to the measured value of ΔM_{FWHM} at 180

MeV. The calculated temperature dependence of ΔM_{FWHM} reproduces the trend of the data rather well. Our observations are, therefore, not inconsistent with the temperature dependence expected for the achievement of statistical equilibrium for the mass asymmetry degree of freedom. This result is in qualitative agreement with recent measurements[13] for the system $^{35}Cl + ^{197}Au$ for which the major energy dependence of the widths of the fission fragment mass distributions could be attributed to the expected temperature dependence.

V. Energy Dependence of Capture Cross Sections

The compound nucleus ^{240}Cf which is formed by the fusion of ^{32}S and ^{208}Pb has a small fission barrier. The solid line in Figure 8 shows the angular momentum dependence of the fission barrier as predicted by the rotating liquid drop model[4]. Slightly lower fission barriers are predicted from the macroscopic two-center model[27] which includes the effects due to the finite range of the nuclear force and to the diffuse nuclear surface (see dashed line in Figure 8). Both models predict that the fission barrier vanishes for angular momenta larger than about 60 $\hbar$.

Because of these low fission barriers, capture reactions of ^{208}Pb and ^{32}S are expected to be followed by fission. The cross section for the formation of particle stable evaporation residues is negligible as compared to the fission cross section. Consequently, the integrated fusion-fission cross section (excluding the contributions from fission following deeply inelastic reactions) is identified with the cross section for capture reactions.

Figure 9 shows the energy dependence of the measured capture cross sections. The dashed curve corresponds to the cross section predicted for the passage over the conditional saddle point in terms of the parameterization of ref. 12. At the higher energies the measured cross sections considerably exceed the predicted cross section indicating that the "extra push" needed for the passage over the conditional saddle point is overestimated for the present system. Similar observations were made[28] for capture reactions of $^{40}Ar + ^{197}Au$. In fact, the measured capture cross sections can be rather well described by classical trajectory calculations using the proximity potential and one-body dissipation[3], as is shown by the solid curve in Figure 9.

The values of the sharp cut-off angular momenta ℓ_c determined from the measured capture cross sections (see eq. 1) are listed in Table I. For energies $E \geq 210$ MeV these angular momenta exceed the value $\ell_{Bf=0} \approx 60\ \hbar$ corresponding to vanishing fission barrier according to the rotating liquid drop model. At least for these higher energies, the reaction is expected to include processes such as fast fission reactions, which do not involve the formation of the compound nucleus. At the same time, one cannot exclude contributions from non-compound processes at energies below 210 MeV since the sharp cut-off approximation is rather unrealistic as, owing to zero-point oscillations of the nuclear surface, angular momenta in excess of the value ℓ_c are expected to contribute to the capture reaction[29,30]. Furthermore, capture beyond the conditional saddle does not ensure passage

over the true saddle point which is a necessary condition for compound nucleus formation.

VI. Angular Distributions

Fission fragment angular distributions contain valuable information about the collective rotations of the composite system prior to scission. In the framework of the transition state model of compound nucleus fission[15,31], the fission fragment angular distribution is determined by the total angular momentum I, its projection M on the space fixed axis, and its projection K on the body fixed symmetry axis that coincides with the direction of fission. By assuming Gaussian shaped K-distributions corresponding to the statistical population of K-states at the saddle point, remarkably good agreement has been obtained for a large body of data[15]. If the compound nucleus is formed by the fusion of two nuclei with zero intrinsic angular momentum the total angular momentum is equal to the orbital angular momentum ℓ of relative motion, $I=\ell$. If the beam axis is chosen as the space fixed quantization axis the fission fragment angular distribution is given by

$$\frac{d\sigma}{d\Omega}(\theta) = \pi\lambda\!\!\!^{-2} \sum_{\ell=o}^{\infty} (2\ell+1)\, T_\ell \frac{\sum_{K=-\ell}^{+\ell} \tfrac{1}{2}(2\ell+1)\, |\mathcal{D}^{\ell}_{M=o,K}(\theta)|^2 \exp(-\frac{K^2}{2K^2_{o,\ell}})}{\sum_{K=-\ell}^{+\ell} \exp(-K^2/2K^2_{o,\ell})} \qquad (4)$$

with

$$K^2_{o,\ell} = T\,\mathcal{J}_{eff}/\hbar^2 = T(\frac{\hbar^2}{\mathcal{J}_{\parallel}} - \frac{\hbar^2}{\mathcal{J}_{\perp}})^{-1}. \qquad (5)$$

Here, T_ℓ denotes the probability of capture for the partial wave of angular momentum ℓ, $\mathcal{D}^{\ell}_{M=o,K}$ is the symmetric top wave function, T is the nuclear temperature, and $\mathcal{J}_{\parallel}$ and $\mathcal{J}_{\perp}$ are the moments of inertia of the saddle point configuration about axes of rotation parallel and perpendicular to the symmetry axis. For simplicity, one often assumes that the variance of the K-distribution is independent of angular momentum, i.e. $K_{o,\ell} = K_o$.

For compound nucleus excitation energies well above the fission barrier, the effective moments of inertia extracted from the analysis of measured fission fragment angular distributions agree, in general, rather well with the saddle point shapes predicted by the rotating liquid drop model[15,32]. Within the context of this model, the effective moments of inertia are expected to decrease with increasing fissility parameter and with increasing angular momentum, because the saddle point shapes become more compact. Thus for more fissile compound nuclei, the liquid drop model predicts angular distributions which are more isotropic, in qualitative agreement with experimental observations[15,32]. Recently, however, the angular distributions measured for ^{32}S induced fusion-fission reactions on heavy targets[16-19] were found to be substantially more anisotropic than expected. The description of these angular distributions in terms of

eq. 4 requires K_o-values which are clearly inconsistent with the saddle point shapes predicted by the rotating liquid drop model.

Although equations 4 and 5 were originally derived to explain angular distributions measured for the fission decay of compound nuclei, they are of more general validity. The equations remain valid as long as the final total helicity distribution reflects a statistical equilibrium distribution of K-values at some intermediate stage of the reaction. For this more general situation, the values of $K_{o,\ell}$ extracted from the analysis of the measured angular distributions provide information about that stage of the reaction at which the K-distribution is frozen. The corresponding configuration may be different from the saddle point configuration.

It can be shown[33] that the angular anisotropy given in terms of eq. 4 depends mainly on the average value of the ratio $\langle \ell/K_{o,\ell} \rangle \approx \langle \ell \rangle / K_o$. Clearly, this ratio depends on the distribution of capture probabilities, T_ℓ, which cannot be predicted reliably. As a consequence, the extracted values of $K_{o,\ell}$ will depend on the particular choice of capture probabilities. Rather significant uncertainties of the extracted $K_{o,\ell}$-values exist at energies close to the barrier where only few, if any, partial waves contribute with full strengths. At higher energies where a large number of partial waves are expected to be captured with unit probability, the extracted $K_{o,\ell}$-values are significantly less ambiguous. A more detailed discussion of these uncertainities is given in Appendix II.

For the present analysis, we assume that the transition of the capture probabilities from T_ℓ=1 to T_ℓ=0 takes place over a comparable number of partial waves as the transition from $T_\ell^{(OM)}$=1 to $T_\ell^{(OM)}$=0 of transmission coefficients obtained from optical model calculations. The nuclear part of the optical potential[18] was parameterized as $U(r) = (V+iW)\ \{1+\exp[(r-R)/a]\}^{-1}$ with V=W=40 MeV, R=10.65 fm and a=0.54 fm. For each energy we used the relation

$$T_\ell = T_{\ell+\ell'}^{(OM)} \qquad (6)$$

and adjusted the parameter ℓ' to reproduce the experimental capture cross section.

The angular distributions measured in the present experiment are shown in Figure 10. With increasing beam energy (and, correspondingly, with larger contributions from angular momenta exceeding $\ell_{Bf=o}$) the angular distributions become more anisotropic. Even at the lowest beam energy, the measured angular distributions are incompatible with the effective moments of inertia of the saddle point configuration predicted by the rotating liquid drop model, as will be discussed in detail in Appendix II.

In the following discussion we analyze the present angular distributions and the ones of ref. 18 in terms of eqs. 4 and 5. In the first step of the analysis we have fit the data assuming an angular momentum independent value of $K_{o,\ell}=K_o$ at each energy. If one assumes that the K-distributions correspond to statistical equilibrium distributions, which are frozen in at a particular deformation, the extracted

value of K_o may be related to the effective moment of inertia at this configuration via eq. 5. For simplicity, the nuclear temperature T was calculated from eq. 3 by neglecting the rotational energy. We used the rigid sphere moment of inertia $\mathcal{J}_o = 133\ \hbar^2\ \mathrm{MeV}^{-1}$ (corresponding to the radius $R_o = 1.2205\ A^{1/3}$ fm) to obtain the dimensionless numbers $\mathcal{J}_o/\mathcal{J}_{eff}$. The resulting best-fit values of $\mathcal{J}_o/\mathcal{J}_{eff}$ are shown in Figure 11 by the open and solid circles. The error bars indicate the range of $\mathcal{J}_o/\mathcal{J}_{eff}$ for which the absolute χ^2-value does not increase by more than one from the best-fit value. For a given energy, the best-fit value of $\mathcal{J}_o/\mathcal{J}_{eff}$ is plotted for the mean square angular momentum $\langle \ell^2 \rangle$ which scales with the average value of the rotational parameter as defined in ref. 4 (see upper scale of the figure). For comparison, the values of $\mathcal{J}_o/\mathcal{J}_{eff}$ predicted by the rotating liquid drop model[4] and the macroscopic two-center model[27] are shown by the solid and dashed curves, respectively. In contrast to the predictions of these models the value of $\mathcal{J}_o/\mathcal{J}_{eff}$ does not go to zero for large angular momenta, but rather towards the constant value of $\mathcal{J}_o/\mathcal{J}_{eff} \approx 1$.

The rather smooth variation of the effective moment of inertia with the mean square angular momentum $\langle \ell^2 \rangle$ suggests that it should be possible to parameterize the effective moment of inertia in terms of a simple function of this variable and use this functional dependence to fit the entire set of angular distributions. For simplicity we have adopted a functional dependence of the form

$$\mathcal{J}_o/\mathcal{J}_{eff} = \begin{cases} a - b\,\ell^2, & \text{for } \ell^2 \leq \frac{a-c}{b} \\ c, & \text{for } \ell^2 > \frac{a-c}{b} \end{cases} \qquad (6)$$

where the parameters a, b and c are chosen to provide a fit to all angular distributions. The solid line in Figure 11 shows this functional dependence for the best set of parameters, $a=2.2$, $b=6.6\times10^{-4}$, $c=1.01$. The corresponding angular distributions, shown by the solid lines in Figure 10, provide an excellent fit to the data. As in our previous calculations with constant value of $K_{o,\ell}=K_o$ the angular momentum dependence of the temperature was neglected. In order to asses the importance of this latter effect, we also performed calculations using the relation

$$T = [8.5\ \mathrm{MeV}(E^* - E_{rot})/A]^{\frac{1}{2}} \qquad (7)$$

where the rotational energy was taken as

$$E_{rot} = \frac{\ell(\ell+1)\hbar^2}{2\mathcal{J}_\perp^e} . \qquad (8)$$

and $\mathcal{J}_\perp^e$ was taken as the moment of inertia of an axially symmetric ellipsoid rotating about an axis perpendicular to the symmetry axis. The shape of this ellipsoid was chosen to reproduce the value of $\mathcal{J}_o/\mathcal{J}_{eff}$ given by eq. 6, and the volume of this ellipsoid was taken as the equivalent sphere volume $V=\frac{4\pi}{3} R_o^2$, with $R_o = 1.2205\ A^{1/3}$ fm. Fits of comparable quality are obtained by this procedure giving a slightly lower value of the asymptotic value $\mathcal{J}_o/\mathcal{J}_{eff} = 0.93$, see the dashed line in Figure 11.

Although the effective moment of inertia cannot be related to a given nuclear deformation in a model independent way, it is instructive to exhibit the values of $\mathcal{J}_o/\mathcal{J}_{eff}$ for two simple families of axially symmetric rigid bodies of uniform density. The light and heavy curves in Figure 12 give the values of $\mathcal{J}_o/\mathcal{J}_{eff}$ for axially symmetric ellipsoids of prolate deformation and for two overlapping spheres. The horizontal axis of the figure is given in terms of the ratio b/a, where b and a denote the maximum dimensions of these objects in the directions parallel and perpendicular to the symmetry axis. Examples of particular shapes are given for the values of $\mathcal{J}_o/\mathcal{J}_{eff}$=0.5, 1.0 and 1.5, respectively. The relatively large values of $\mathcal{J}_o/\mathcal{J}_{eff} \gtrsim 1.0$ obtained from the present analysis imply that the K-distributions are frozen in at rather large deformations corresponding to $b/a \gtrsim 2$.

It was shown in ref. 18 that the fusion-fission angular distributions measured for the system $^{16}O + ^{238}U$ are consistent with the expectations from the rotating liquid drop model. The compound nuclei formed in the $^{32}S + ^{208}Pb$ and $^{16}O + ^{238}U$ reactions have very similar fissility parameters, x=0.837 and x=0.842. It is, therefore, difficult to reconcile the large values of $\mathcal{J}_o/\mathcal{J}_{eff}$ extracted for the $^{32}S + ^{208}Pb$ reaction with the concept of compound nucleus formation followed by fission and it was suggested[18] that the spherical compound nucleus configuration might never be achieved for this reaction. The reaction was, therefore, suggested to proceed via passage over the conditional saddle point rather

than passage over the true fission saddle point, corresponding to the occurrence of fast fission, even at energies close to the barrier.

At the higher energies of E_{lab}=250 and 266 MeV, a major part of the capture cross section involves angular momenta corresponding to vanishing liquid drop fission barrier for which the process of fast fission is also expected to occur. The consistent description of several angular distributions over a large range of energies in terms of a simple functional dependence of the effective moment of inertia on angular momentum and the large values of $\mathcal{J}_o/\mathcal{J}_{eff}$ are consistent with the assumption (but do not prove) that the present fast fission reaction proceeds via rather elongated shapes for sufficiently long times to attain thermal equilibrium distributions of the angular momentum projection along the scission axis.

At present, experimental evidence[15,16,32] is consistent with the assumption that the K-distribution is frozen in at the saddle point for the case of normal compound nucleus fission with insignificant reorganization taking place as the system proceeds from the saddle point to scission. It then appears unlikely that fast fission processes attain the more compact saddle point shapes for a sufficient amount of time to attain statistical K-distributions. Indeed, if more compact shapes are obtained for fast fission reactions an alternate interpretation[34] of the narrow K-distributions will have to be taken into consideration. It is conceivable that the reaction may proceed so rapidly that the reaction

products are primarily emitted in the reaction plane defined by the initial impact parameter. In that case, the K-distributions would be determined by the reaction dynamics and should not be interpreted in terms of statistical equilibrium distributions. It is more difficult to perform quantitative calculations for this latter assumption. Clearly, more systematic data on fast fission are called for to search for possible violations of the assumption of statistical K-distributions which was found to be consistent with the present set of data.

VII. Summary

In order to search for possible experimental signatures of fast fission processes we have studied fission following capture reactions induced by ^{32}S on ^{208}Pb over the energy range of E_{lab}=180 - 270 MeV. Over this range of energies, the maximum angular momentum for capture ℓ_c, obtained in the sharp cut-off approximation, increases from values considerably smaller to values significantly larger than the angular momentum $\ell_{Bf=o}$ for which the fission barrier is expected to vanish.

From the measurement of the distribution of folding angles between coincident fission fragments it was confirmed that the reaction proceeds via the capture of essentially the entire projectile by the target nucleus. At the highest energies investigated, there is evidence for the occurrence of deeply inelastic reactions followed by sequential fission

of the target residue. Except at backward angles this process is separated kinematically from fission following capture reactions. Possible contributions of sequential fission to the experimental capture cross sections are within the quoted errors.

The widths of the fission fragment mass distributions, ΔM_{FWHM}, were found to increase rather smoothly with increasing beam energy. Within our experimental uncertainties, we did not find positive evidence for an abrupt increase of ΔM_{FWHM} for $\ell_c > \ell_{Bf=o}$. Rather, our observations are consistent with the expected variation of ΔM_{FWHM} with temperature. Even for low angular momenta the compound nucleus ^{240}Cf has a small fission barrier which gradually goes to zero for $\ell \to \ell_{Bf=o}$. Because of this smooth decrease of the fission barrier with increasing angular momentum and because of the high excitation energies of the composite system it appears unlikely that dramatic effects should be observed in the vicinity of $\ell_c \sim \ell_{Bf=o}$. Since the sharp cut-off model is unrealistic, additional smearing of any discontinuities is expected to occur due to the finite range of ℓ-values for which the partial wave capture probabilities decrease from T_ℓ=1 to T_ℓ=0.

The energy dependence of the capture cross section can be rather well described in terms of classical trajectory calculations[3] using the proximity potential and one-body dissipation. At the highest energies, the capture cross sections are larger than predicted from a recent parameterization[12] of the cross section corresponding to the passage over the

conditional saddle point indicating that the "extra push" needed for the passage over the conditional saddle point is overestimated for the present system.

Even at the lowest energy of E_{lab}=180 MeV, where the reaction should be expected to proceed via compound nucleus formation followed by fission, the angular distribution cannot be described by the transition state model if predicted[4,27] saddle point deformations are used. We have analyzed the angular distributions by making the assumption that the final total helicity distribution corresponds to a statistical equilibrium distribution of K-values at some intermediate stage of the reaction. By adopting a simple functional dependence of the effective moment of inertia on angular momentum, a consistent description of the measured angular distributions was achieved. The extracted values of $\mathcal{J}_o/\mathcal{J}_{eff}$ indicate that the distribution of K-values is frozen in at rather large deformations. Since these findings are difficult to understand in terms of the systematic trends established for compound nucleus formation and fission decay, it was suggested[18] that the present reaction might proceed via fast fission even at the lowest energies. Obviously, more systematic investigations for different systems will be necessary to substantiate the assumptions on which the present analysis and interpretation are based. Of particular importance is the question whether the extracted narrow K-distributions correspond to equilibrium distributions of some intermediate stage of the reaction or whether they are governed by non-equilibrium dynamical effects.

Finally, we should point out that our analysis was based on the assumption of first chance fission. At present, there is no quantitative experimental information available to determine whether this assumption is correct. Recent schematic studies[35] of the effects of light particle emission prior to fission indicate that the qualitative results of our analysis are unlikely to be affected even if higher chance fission were not entirely negligible for the present reaction.

Appendix I. Kinematic transformations and correction for neutron evaporation.

A. Angular Distributions:

The following approximations were used for the extraction of fission fragment angular distributions in the center-of-mass frame. For a given laboratory angle, the fusion-fission cross section was integrated over mass and energy, giving the fission fragment differential cross section $d\sigma_{f,lab}/d\Omega$. The resulting angular distribution was transformed into the center-of-mass system by assuming symmetric fission of the compound nucleus and a total kinetic energy release (in the center-of-mass frame) of TKE=188 MeV derived from the systematics of ref. 26. By adopting this procedure, the variation of the kinematic transformation over the finite range of fission fragment velocities is neglected. Although we have not assessed the error introduced by this procedure, it is likely to be small since the resulting angular distributions were found to be symmetric about θ_{cm}=90° within

the accuracy of the present experiment, see Figure 11. (Note, that the mass and energy integrated angular distributions must be symmetric about 90° in the center-of-mass system, since each fragment emitted at an angle θ_1 is accompanied by a fragment emitted at the angle $\theta_2 = \pi - \theta_1$.)

B. Mass Distributions:

To extract the primary fission fragment mass distributions we used the following procedure.

The scattering angle θ_ℓ, the velocity V_ℓ, and the kinetic energy E_ℓ of fission fragments were measured in the laboratory. (For clarity we will refer to these fragments as secondary fission fragments and to fragments prior to neutron evaporation as primary fission fragments.) Using the measured velocity and energy, the mass number of the secondary fragment, M', is obtained via

$$M' = 2E_\ell/m_o V_\ell^2 \qquad \text{(A-1)}$$

where m_o is the nucleon mass.

Assuming that the velocity of a fission fragment is not changed by neutron evaporation the velocity, V_{cm}, and the scattering angle, θ_{cm}, of fission fragments in the center-of-mass system are given by

$$V_{cm}^2 = V_\ell^2 + V_o^2 - 2\, V_\ell\, V_o \cos\theta_\ell\,, \qquad \text{(A2)}$$

$$\cos\theta_{cm} = (V_\ell \cos\theta_\ell - V_o)/V_{cm}\,, \qquad \text{(A3)}$$

$$V_o = (2M_p\, E_p/m_o)^{\frac{1}{2}}/M_{cn}. \qquad \text{(A4)}$$

Here, V_o is the velocity of the center-of-mass in the laboratory and E_p, M_p and M_{cn} denote the beam energy, and the mass numbers of the projectile and the compound nucleus, respectively. The total kinetic energy release in the center-of-mass system is related to the primary fragment mass number M, by

$$TKE = \frac{M_{CN}\, M\, m_o}{2(M_{CN}-M)}\, V_{cm}^2. \qquad \text{(A5)}$$

Assuming that the two primary fission fragments have the same temperature, one obtains for the excitation energy of the primary fragment

$$E^*(M) = \frac{M}{M_{CN}}\,(E^*_{CN} + Q - TKE), \qquad \text{(A6)}$$

where E^*_{CN} denotes the excitation energy of the compound nucleus and

$$Q = E_B(M_{CN}, Z_{CN}) - E_B(M_{CN}-M, Z_{CN}-Z). \qquad \text{(A7)}$$

The Q-value was then calculated by assuming liquid droplet binding energies[36]

$$E_B(M, Z) = -a_v M + a_s M^{2/3} + a_c Z^2/M^{1/3} + a_{sym}\frac{(M-2Z)^2}{M} \quad (A8)$$

with:

$a_v = 15.68$ MeV,
$a_s = 18.56$ MeV,
$a_c = 0.717$ MeV,
$a_{sym} = 28.1$ MeV.

Since the fragment charge number Z is not measured in this experiment, Green's approximation to the valley of stability was used to relate it to the mass number M' of the detected secondary fission fragment:

$$Z = M' / (2+0.0128\ M'^{2/3}). \quad (A9)$$

For an evaporation spectrum of the form

$$\frac{dN}{dE} = C\ E\ e^{-E/T} \quad (A10)$$

the average kinetic energy of the emitted particles is

$$\langle E_K \rangle = 2T. \quad (A11)$$

The average number of neutrons n emitted from the primary fragment may then be estimated as

$$n(M) = E^*(M) / (B_n+2T) \quad (A12)$$

where B_n denotes the average neutron separation energy. For simplicity, the constant value of B_n=6.5 MeV was used. The temperature was taken at $T = (8.5\ E^*(M)/M)^{\frac{1}{2}}$. An iterative procedure was used to achieve internal consistency with the relation n(M)=M-M'.

In order to correct for possible kinematic distortions of the mass distributions measured in the laboratory we assumed that the fission cross section in the center-of-mass system is of the form

$$\frac{d^3\sigma}{dM dE_{cm} d\Omega_{cm}}(E_{cm}, \theta_{cm}, M) = \frac{d^2\sigma}{dM dE_{cm}} \frac{1}{\sin\theta_{cm}} . \quad (A13)$$

Since the mass distributions were determined for rather large scattering angles, this approximation is quite good.

The mass distribution $\frac{d\sigma}{dM}$, is then obtained by

$$\frac{d\sigma}{dM} = \int_0^\infty \frac{d^2\sigma}{dM dE_{cm}} dE_{cm}. \quad (A14)$$

The measured center-of-mass cross section is given by[37]

$$\frac{d^3\sigma}{dM dE_{cm} d\Omega_{cm}}(E_{cm,k}, \theta_{cm}, M) = \text{const}\ \frac{N_k(M)}{\Delta E_{cm}} \frac{V_{cm}}{V_\ell} (1 - \frac{V_o \cos\theta_\ell}{V_\ell}) \frac{1}{\Delta\Omega_\ell} \quad (A15)$$

where $N_k(M)$ denotes the number of fission fragments detected with center-of-mass energies in the energy interval $(E_{cm,k} - \Delta E_{cm}/2; \Delta E_{cm,k} + E_{cm}/2)$ and $\Delta\Omega$ is the detector solid angle in the laboratory. Combining eqs. A13-A15, one obtains for the mass distribution

$$\frac{d\sigma}{dM} = \sum_k \frac{N_k(M) V_{cm} \sin\theta_{cm}}{V_\ell} \left(1 - \frac{V_o \cos\theta_\ell}{V_\ell}\right) \frac{1}{\Delta\Omega_\ell} . \quad (A16)$$

Appendix II. Sensitivity to the partial wave distribution at near barrier energies

In order to assess the uncertainties that have to be associated with the unknown angular momentum dependence of the capture probabilities we used the following parameterization[38]

$$T_\ell = 1 - \{ 1+\exp[(\ell_o - \ell)/\Delta]\}^{-2} . \quad (A17)$$

Examples of the partial wave capture cross sections calculated with this parameterization are given in Figure 13 and 14. For a given choice of Δ, the value of ℓ_o is taken to reproduce the measured capture cross section. In the sharp cut-off limit, $\Delta=0$, one has $\ell_c=\ell_o$. For orientation, the upper horizontal scales of the figures give the reduced distance of closest approach, $d_o=d_{min}\,(A_T^{1/3}+A_p^{1/3})^{-1}$, calculated for pure Coulomb trajectories from the semi-classical relation

$$\ell(\ell+1) = k^2\, d_{min}^2 - 2k\, d_{min}\, \eta. \quad (A18)$$

where $k=p/\hbar$ is the wave number of relative motion and $\eta=z_p\, z_T\, e^2/\hbar v$ is the Coulomb parameter. As is apparent from the two figures, the values of $\Delta=10$ and $\Delta=15$ represent rather drastic deviations from the classical sharp cut-off model for capture. The corresponding partial wave capture

cross sections may, however, not be entirely unrealistic. In fact, comparably broad distributions are predicted[29,30] if the zero point oscillations of the nuclear radii and shapes are taken into account. Similarly, rather broad distributions of partial wave capture cross sections are obtained by the prescription of eq. 6 which was adopted for the analysis of the energy dependence of the angular distributions.

In the first part of the analysis described in the main text we fit the experimental angular distributions with an angular momentum independent value of $K_{o,\ell}=K_o$. In order to assess the ambiguities of the extracted values of K_o, we performed similar calculations using the parameterization of eq. A17 for the partial wave fusion probabilities T_ℓ. Examples of such calculations are shown in Figure 15. The light and heavy solid lines correspond to calculations performed with the parameters of $K_o=7.5$, $\Delta=0$ and $K_o=9.5$, $\Delta=10$, respectively. The fits to the data are excellent. Fits of similar quality are obtained at higher energies.

The best fit values of K_o depend on the cut-off parameter Δ used for the parameterization of the fusion probabilities. As is shown in Figure 16, the use of broader distributions of the partial wave fusion cross section results in enhanced values of K_o. This effect is particularly pronounced at the lower energies and may result in sizeable uncertainties for the analysis of angular distributions at energies close to the barrier unless independent information on the angular momentum dependence of the fusion probability is available.

At higher energies, the dependence of the best fit value of K_o on the width parameter Δ is less pronounced. For the present system, this dependence is of minor importance at incident energies above 210 MeV.

At the lowest energy investigated in this experiment, E_{lab}=180 MeV, the sharp cut-off angular momentum for capture, ℓ_c=31 $\hbar$, is significantly smaller than the value of $\ell_{Bf=0} \approx$ 60 $\hbar$ for which the fission barrier vanishes. At this energy, the reaction should be expected to proceed via compound nucleus formation and fission decay. However, even at this low energy the measured angular distribution cannot be understood in terms of the transition state model if effective moments of inertia are used that correspond to the saddle point shapes predicted by the rotating liquid drop[4] and the macroscopic two-center[27] models. To demonstrate this point, detailed calculations with the two-center model were performed at this energy. Similar results were obtained by interpolating the saddle point shapes published for the rotating liquid drop model. For each angular momentum, the effective moment of inertia and the temperature of the saddle point configuration were calculated. The corresponding values of $K_{o,\ell}$ are shown in Figure 17. Due to numerical uncertainties the values of $K_{o,\ell}$ corresponding to angular momenta larger than 45 $\hbar$ have been extrapolated to give $\mathcal{J}_{eff}^{-1} \to 0$ for $\ell \to 64$ $\hbar$ (see also Figure 11 for the corresponding values of $\mathcal{J}_o/\mathcal{J}_{eff}$). It was verified that our conclusions are not affected by the uncertainties inherent in this extrapolation.

The light and heavy dashed curves of Figure 15 represent

calculations using these values of $K_{o,\ell}$ and the T_ℓ-values according to eq. A17 for Δ=0 and Δ=10, respectively. None of these model calculations reproduces the large angular anisotropies observed experimentally.

The uncertainties that arise from the unknown distribution of partial wave capture probabilities are not sufficiently large to account for the failure of the transition state model to reproduce the observed large angular anisotropies in terms of predicted saddle point deformations. This is apparent from the thin dashed lines in Figure 17 which show the best-fit values of K_o obtained for the parameters Δ=0, 10 and 15. Even for the extreme value of Δ=15 the best-fit parameter of $K_o = 11.75 \pm 0.7$ is significantly smaller than the minimum value of $K_{o,\ell} \approx 15$ obtained from the macroscopic two-center model at low angular momenta.

Acknowledgements

One of us (D.A.) acknowledges the support he received from NATO and Michigan State University and thanks the National Superconducting Cyclotron Laboratory for its hospitality and another (C.K.G.) acknowledges the partial support of the Alfred P. Sloan Foundation. This work was supported by the U.S. Department of Energy and by the National Science Foundation under Grant No. 80-17605.

References

*On leave from University of Nantes (France); now at: G.A.N.I.L. (France).

1. B. Heusch, C. Volant, H. Freiesleben, R.P. Chestnut, K.D. Hildenbrand, F. Pühlhofer, W.F.W. Schneider, B. Kohlmeyer, and W. Pfeffer, Z. Phys. A288, 391 (1978).

2. C. Lebrun, F. Hanappe, J.F. Lecolley, F. Lefebvres, C. Ngô, J. Péter, and B. Tamain, Nucl. Phys. A321, 207 (1979).

3. J.R. Birkelund, L.E. Tubbs, J.R. Huizenga, J.N. De, and D. Sperber, Phys. Reports 56, 107 (1979).

4. S. Cohen, F. Plasil, and W.J. Swiatecki, Ann. Phys. 82, 557 (1974).

5. B. Borderie, M. Berlanger, D. Gardès, F. Hanappe, L. Nowicki, J. Péter, B. Tamain, S. Agarwal, J. Girard, C. Grégoire, J. Matuszek, and C. Ngô, Z. Phys. A299, 263 (1981).

6. C. Grégoire, C. Ngô, and B. Remaud, Phys. Lett. 99B, 17 (1981).

7. C. Grégoire, R. Lucas, C. Ngô, B. Schürmann, and H. Ngô, Nucl. Phys. A361, 443 (1981).

8. C. Grégoire, C. Ngô, and B. Remaud, Nucl. Phys. A383, 392 (1982).

9. W.J. Swiatecki, Physica Scripta 24, 113 (1981).

10. W.J. Swiatecki, Nucl. Phys. A376, 275 (1982).

11. S. Bjørnholm and W.J. Swiatecki, Nucl. Phys. A391 471.

12. R. Bock, Y.T. Chu, M. Dakowski, A. Gobbi, E. Grosse, A. Olmi, H. Sann, D. Schwalm, U. Lynen, W. Müller, S. Bjørnholm, H. Esbensen, W. Wölfli, and E. Morenzoni, Nucl. Phys. A388, 334 (1982).

13. V. Bernard, C. Grégoire, C. Ngô, M. Ribrag, G.Y. Fan, H. Ho, W. Kühn, and J.P. Wurm, Nucl. Phys. A385 319 (1982).

14. M.E. Faber, Phys. Rev. C24, 1047 (1981).

15. R. Vandenbosch and J.R. Huizenga, Nuclear Fission, Academic Press, New York (1973).

16. B.B. Back, H.-G. Clerc, R.R. Betts, B.G. Glagola, and B.D. Wilkins, Phys. Rev. Lett. 46, 1068 (1981).

17. B.B. Back, R.R. Betts, K. Cassidy, B.G. Glagola, J.E. Gindler, L.E. Glendenin and B.D. Wilkins, Proceedings of the Intl. Conference on Nucleus-Nucleus Collisions, held at East Lansing, Sept. 26-Oct. 1, 1982, Vol. 1, p. 110.

18. B.B. Back, R.R. Betts, K. Cassidy, B.G. Glagola, J.E. Gindler, L.E. Glendenin, and B.D. Wilkins, to be published.

19. M.B. Tsang, D. Ardouin, B.B. Back, P.A. Baisden, R. Betts, C.K. Gelbke, W.G. Lynch, M.A. McMahan, S. Saini and Z. Xu, Proceedings of the Intl. Conference on Nucleus-Nucleus Collisions, held at East Lansing, Sept. 26-Oct. 1, 1982, Vol. 1, p. 118.

20. H. Henschel, H. Hipp, A. Kohnle and F. Gönnenwein, Nucl. Instr. and Meth. 125, 365 (1975).

21. H.W. Schmitt and R.B. Leachman, Phys. Rev. 102, 183 (1956).

22. T. Sikkeland, E.L. Haines, and V.E. Viola, Jr., Phys. Rev. 125, 1350 (1962).

23. B.B. Back, K.L. Wolf, A.C. Mignerey, C.K. Gelbke, T.C. Awes, H. Breuer, V.E. Viola, Jr., and P. Dyer, Phys. Rev. C22, 1927 (1980).

24. V.E. Viola, Jr., B.B. Back, K.L. Wolf, T.C. Awes, C.K. Gelbke, and H. Breuer, Phys. Rev. C26, 178 (1982).

25. E. Duek, L. Kowalski, M. Rajagopalan, J.M. Alexander, D. Logan, M.S. Zisman, and M. Kaplan, Z. Phys. A307, 221 (1982).

26. V.E. Viola, Jr., Nucl. Data A1, 391 (1966).

27. M.G. Mustafa, P.A. Baisden, and H. Chandra, Phys. Rev. C25, 2524 (1982).

28. E. Duek, L. Kowalski, M. Rajagopalan, J.M. Alexander, T.W. Debiak, D. Logan, M. Kaplan, M. Zisman, and Y. LeBeyec, Z. Phys. A307, 237 (1982).

29. H. Esbensen, Nucl. Phys. A352, 147 (1981).

30. H. Esbensen, private communication.

31. A. Bohr, in Proceedings of the United Nations Intl. Conference on the Peaceful Uses of Atomic Energy, Geneva 1955 (United Nations, New York, 1956), Vol. 2, p. 151.

32. L.C. Vaz and J.M. Alexander, preprint, 1983, and to be published.

33. J.A. Wheeler, in "Fast Neutron Physics", eds. J.B. Marion and J.L. Fowler, Interscience, New York, 1963, Vol. II, p. 2051.

34. K.T. Lesko, S. Gil, A. Lazzarini, V. Metag, A.G. Seamster, and R. Vandenbosch, to be published.

35. H. Rossner, D. Hilscher, E. Holub, G. Ingold, U. Jahnke, H. Orf, J.R. Huizenga, J.R. Birkelund, W.U. Schröder, and W.W. Wilcke, University of Rochester preprint UR-NSRL-260, 1982, and to be published.

36. A. De Shalit and H. Feshbach, Theoretical Nuclear Physics, John Wiley and Sons, Inc., New York, 1974, Vol. 1, p. 126.

37. H.Ho and P.L. Gonthier, Nucl. Instr. and Meth. 190, (1981) 75.

38. F. Videbaek, R.B. Goldstein, L. Grodzins, S.G. Steadman, T.A. Belote, and J.D. Garrett, Phys. Rev. C15, (1977) 954.

Figure Captions

Fig. 1. Experimental setup.

Fig. 2. Most probable folding angle measured between two coincident fission fragments for ^{32}S induced reactions on ^{208}Pb at different incident energies. The dashed lines show the folding angles calculated for symmetric fission of ^{240}Cf nuclei recoiling with 80, 90 and 100% of the beam momentum.

Fig. 3. Scatter plot of the measured folding angle vs. fragment mass for the reaction ^{208}Pb (^{32}S,f)f at E_{lab}=270 MeV.

Fig. 4. Contour plot of mass vs. energy measured for the reaction $^{208}Pb(^{32}S,f)$ at E_{lab}=266 MeV and θ_{lab}=40°.

Fig. 5. Upper part of the figure: Mass dependence of the average value (solid curve) and variance (vertical bars) of the estimated number of neutrons emitted from the primary fission fragments. Lower part of the figure: Primary (circles) and secondary (triangles) mass distributions for fusion-fission reactions induced by ^{32}S on ^{208}Pb at 180 and 266 MeV.

Fig. 6. Mass distributions of primary fission fragments measured for fusion-fission reactions induced by ^{32}S on ^{208}Pb at E_{lab}=180, 210, 250 and 266 MeV. The mass spectra measured at several angles were added to increase statistical accuracy.

Fig. 7. Dependence of the full width at half maximum, ΔM_{FWHM}, of primary fragment mass distributions on the sharp cut-off angular momentum for fusion-fission reactions induced by $^{32}S+^{208}Pb$. The dashed and dot-dashed lines show the expected temperature dependence of the width of the mass distribution normalized to the data at E_{lab}=180 MeV.

Fig. 8. Angular momentum dependence of the fission barrier of ^{240}Cf as predicted by the rotating liquid drop model[4] (solid curve) and the macroscopic two-center model[27] (dashed curve).

Fig. 9. Energy dependence of fusion-fission cross section for ^{32}S induced reactions on ^{208}Pb. The solid curve corresponds to the calculated capture cross section using the proximity potential and one-body dissipation[3]. The dashed curve corresponds to the predicted cross section for the passage over the conditional saddle point in terms of the parameterization of ref. 12.

Fig. 10. Fission fragment angular distributions measured for fusion-fission reactions induced by ^{32}S on ^{208}Pb at E_{lab}=180, 210, 250 and 266 MeV. The dashed curve corresponds to an angular dependence of $1/\sin\theta$. The solid curves have been calculated in terms of eqs. 4, 5 and 6 as described in Section VI.

Fig. 11. Angular momentum dependence of $\mathcal{J}_o/\mathcal{J}_{eff}$, where $\mathcal{J}_o=133\hbar^2$ MeV^{-1} was used for the moment of inertia of the rigidly rotating spherical compound nucleus ^{240}Cf. The solid and dashed curves correspond to the saddle point shapes predicted from the rotating liquid drop model[4] and the macroscopic two-center model[27], in which sharp and diffuse nuclear surfaces are assumed, respectively. The solid and dashed lines correspond to the parameterization eq. 6 of the effective moment of inertia used to fit the energy dependence of the angular distributions as described in the text. The open and solid points represent fits to the angular distributions at different energies with fixed values of $K_{o,\ell}=K_o$. These points are plotted for the average value of the rotational parameter y of the rotating liquid drop model[4], given by the upper scale in the figure.

Fig. 12. Values of $\mathcal{J}_o/\mathcal{J}_{eff}$ for axially symmetric rigid objects of uniform density for two families of shapes corresponding to overlapping spheres (thin lines) and axially symmetric ellipsoids (thick lines). The ratio b/a denotes the ratio of maximum dimensions b and a of these objects in the directions parallel and perpendicular to the symmetry axis, respectively. $\mathcal{J}_o$ denotes the moment of inertia of a rigid sphere of identical density and volume. Examples of particular shapes are given for values of $\mathcal{J}_o/\mathcal{J}_{eff}$=0.5, 1.0, 1.5. The ratio b/a=1 corresponds to a sphere.

Fig. 13. Partial wave capture cross sections corresponding to the parameterization of eq. A17 for the partial wave capture probabilities for ^{32}S induced reactions on ^{208}Pb at 180 MeV. The thick solid line has been obtained from optical model calculations using the prescription of eq. 6. The upper scale gives the reduced distance of closest approach for classical Coulomb trajectories.

Fig. 14. Partial wave capture cross sections corresponding to the parameterization of eq. A17 for the partial wave capture probabilities for ^{32}S induced reactions on ^{208}Pb at 210 MeV. The thick solid line has been obtained from optical model calculations using the prescription of eq. 6. The upper scale gives the reduced distance of closest approach for classical Coulomb trajectories.

Fig. 15. Fission fragment angular distribution measured for fusion-fission induced by ^{32}S on ^{208}Pb at E_{lab}=180 MeV. The dashed curves correspond to angular distributions predicted in terms of the transition state model using the saddle point moments of inertia as predicted by the macroscopic two-center model of ref. 27. The solid curves are fits to the data assuming a constant value of $K_{o,\ell}=K_o$. The partial wave capture probabilities T_ℓ have been parameterized in terms of eq. A17. Thin lines correspond to Δ=0, heavy lines correspond to Δ=10.

Fig. 16. Dependence of the best fit parameters K_o on the width Δ of the partial wave capture probability as parameterized in terms of eq. A17. Calculations have been performed for fusion-fission reactions induced by ^{32}S on ^{208}Pb at E_{lab}=180 and 210 MeV.

Fig. 17. The solid curve shows the angular momentum dependence of $K_{o,\ell}$ calculated for fission of ^{240}Cf at an excitation energy of 50 MeV in terms of the macroscopic two-center model of ref. 27. The dotted part of the curve shows the extrapolated values of $K_{o,\ell}$. The dashed lines give the best-fit parameters $K_o=K_{o,\ell}$ for different width parameters of the partial wave capture probability T_ℓ as defined by eq. A17.

Table I. Laboratory energy E_{lab}, center-of-mass energy E_{cm}, compound nucleus excitation energy E*, capture cross section σ_f and maximum angular momentum for capture ℓ_c, obtained in the sharp cut-off limit, for the present experiment.

E_{lab}(MeV)	E_{cm}(MeV)	E*(MeV)	σ_f(mb)+	$\ell_c(\hbar)$+
180	156	50	150 ± 8	30.4 ± 0.9
190	165	59	292 ± 44	44.1 ± 3.6
200	173	67	480 ± 72	58.3 ± 4.6
210	182	76	604 ± 30	67.1 ± 1.7
230	199	93	866 ± 130	84.4 ± 6.7
250	217	111	968 ± 50	93.1 ± 2.5
266	231	125	1108 ± 55	102.9 ± 2.7
270	234	128	1116 ± 67	104.0 ± 3.2

+Only relative errors are given; the absolute errors are 10% for σ_f and 5% for ℓ_c.

MSUX-83-024

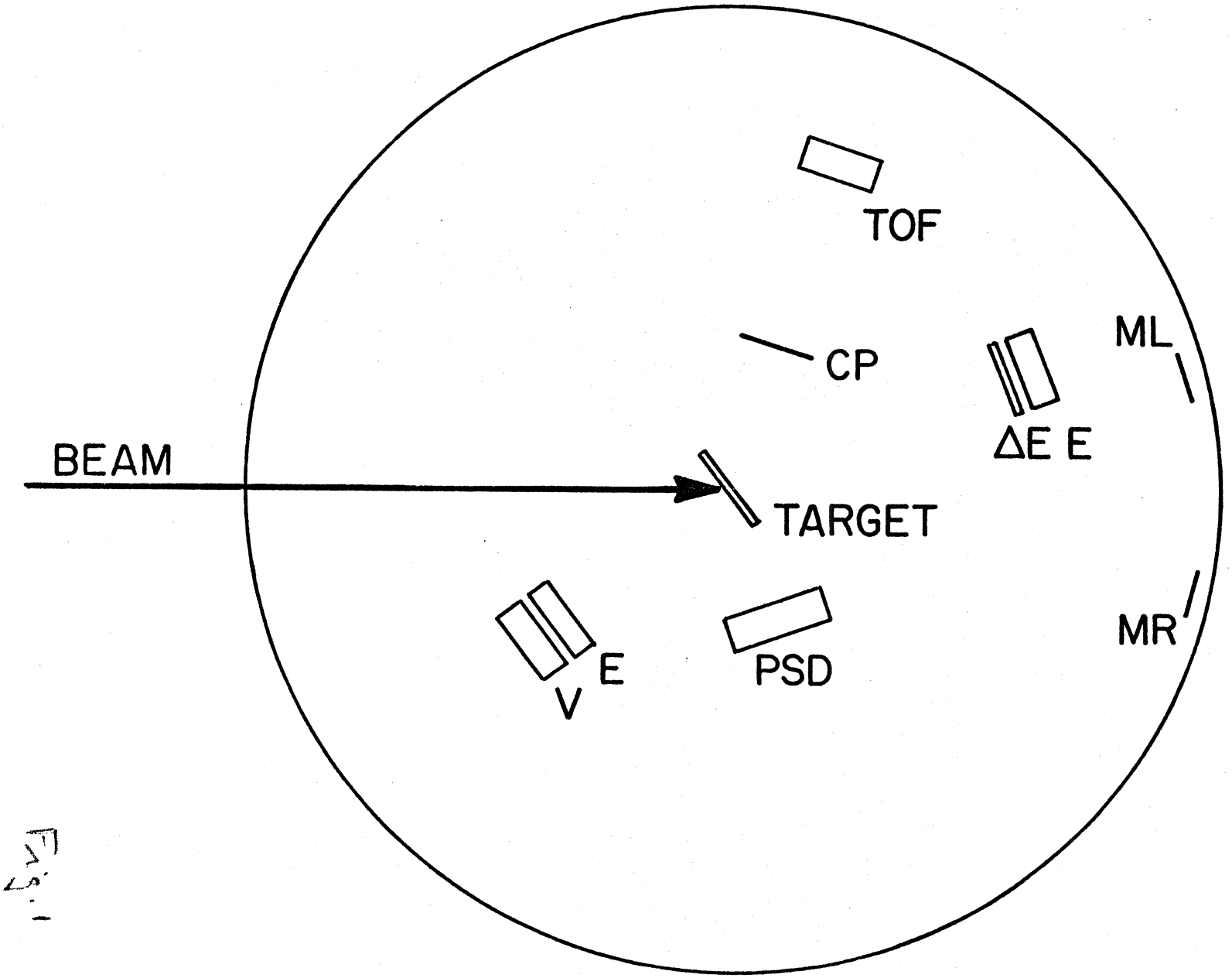

MSUX-82-174

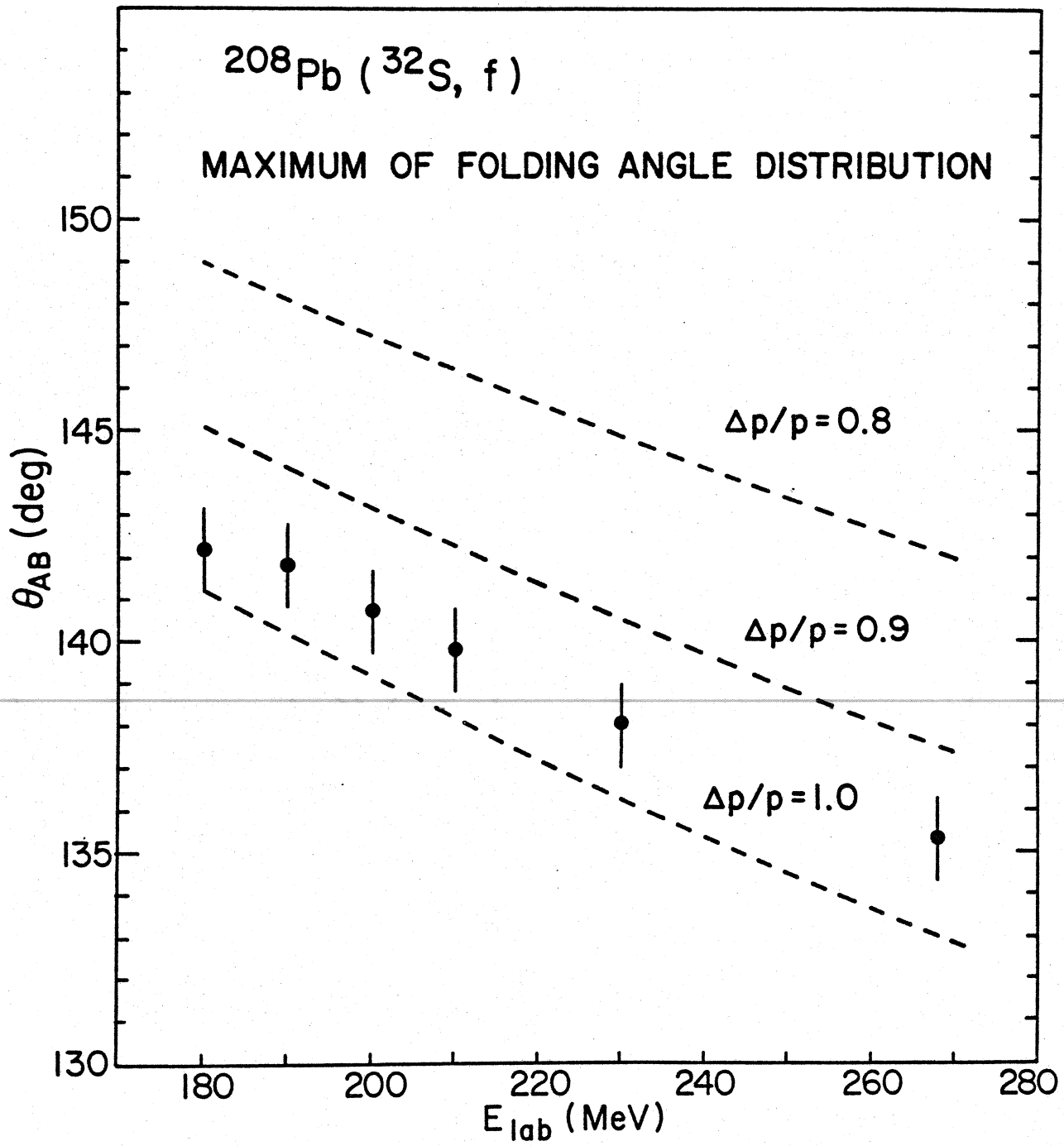

Fig. 2

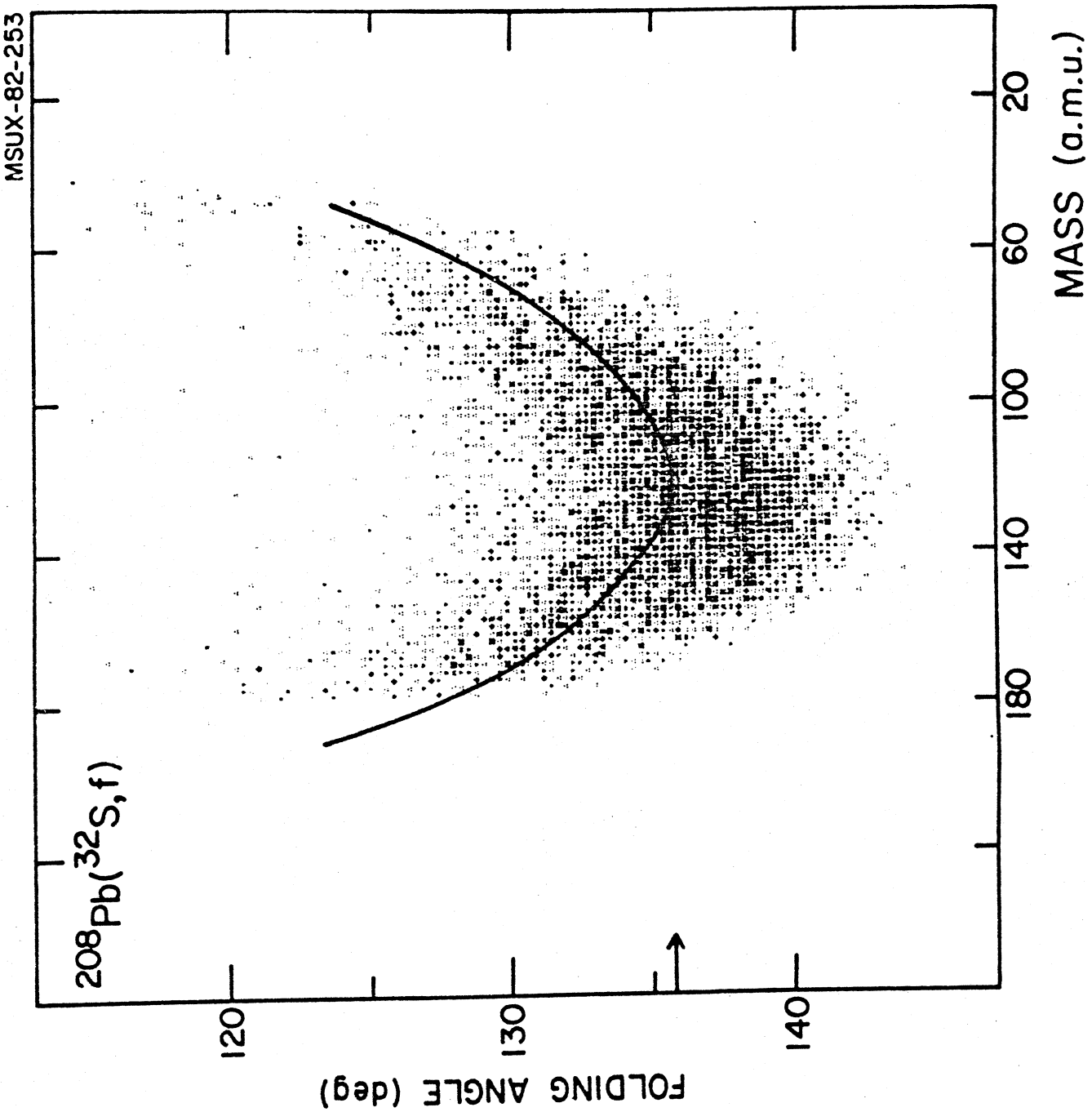
MSUX-82-253
$^{208}Pb(^{32}S,f)$
FOLDING ANGLE (deg)
120
130
140
MASS (a.m.u.)
20
60
100
140
180

Fig. 3

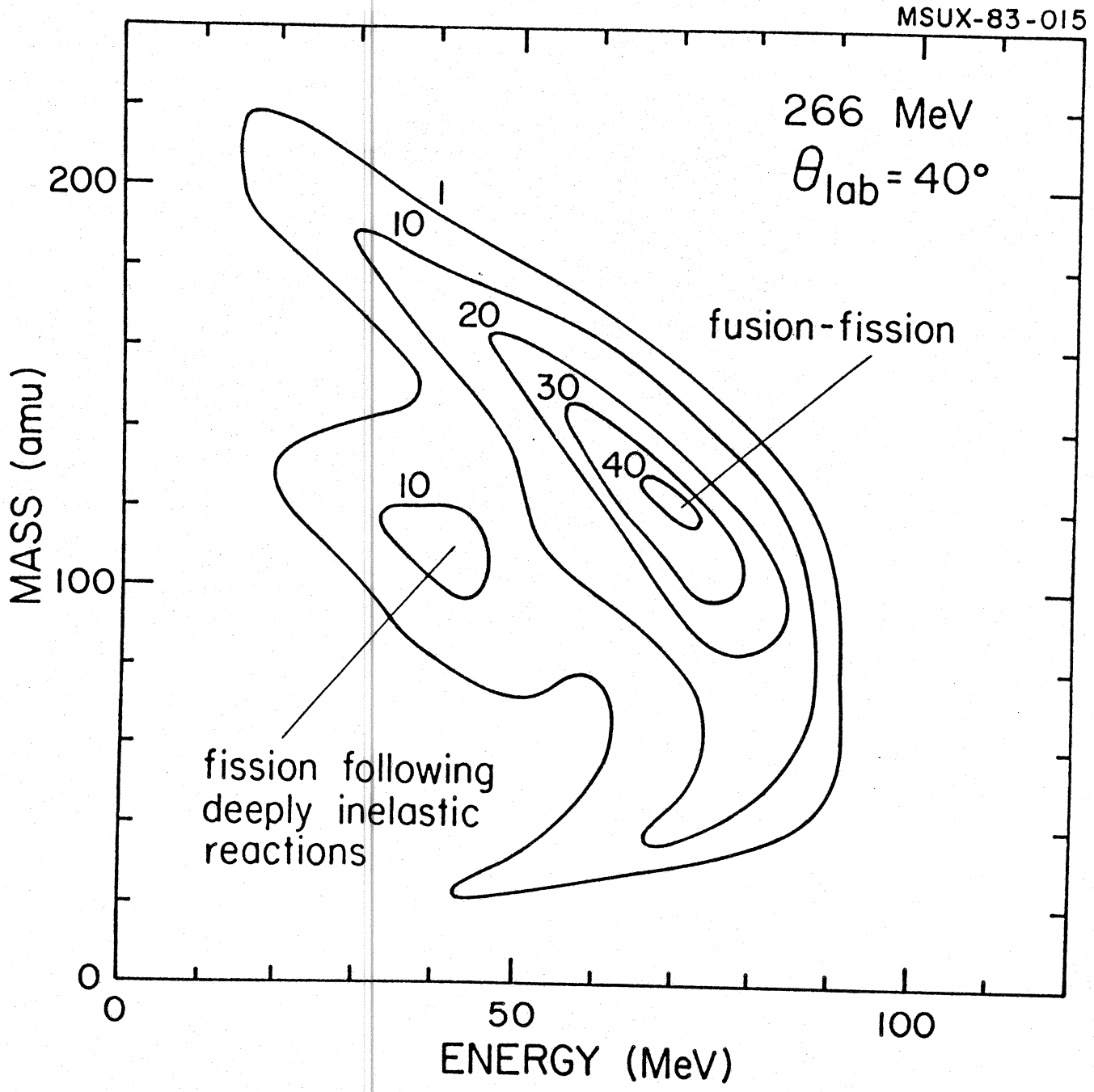
MSUX-83-015
266 MeV
$\theta_{lab} = 40°$
1
10
20
30
40
10
fusion-fission
fission following
deeply inelastic
reactions
MASS (amu)
200
100
0
0
50
100
ENERGY (MeV)

Fig. 4

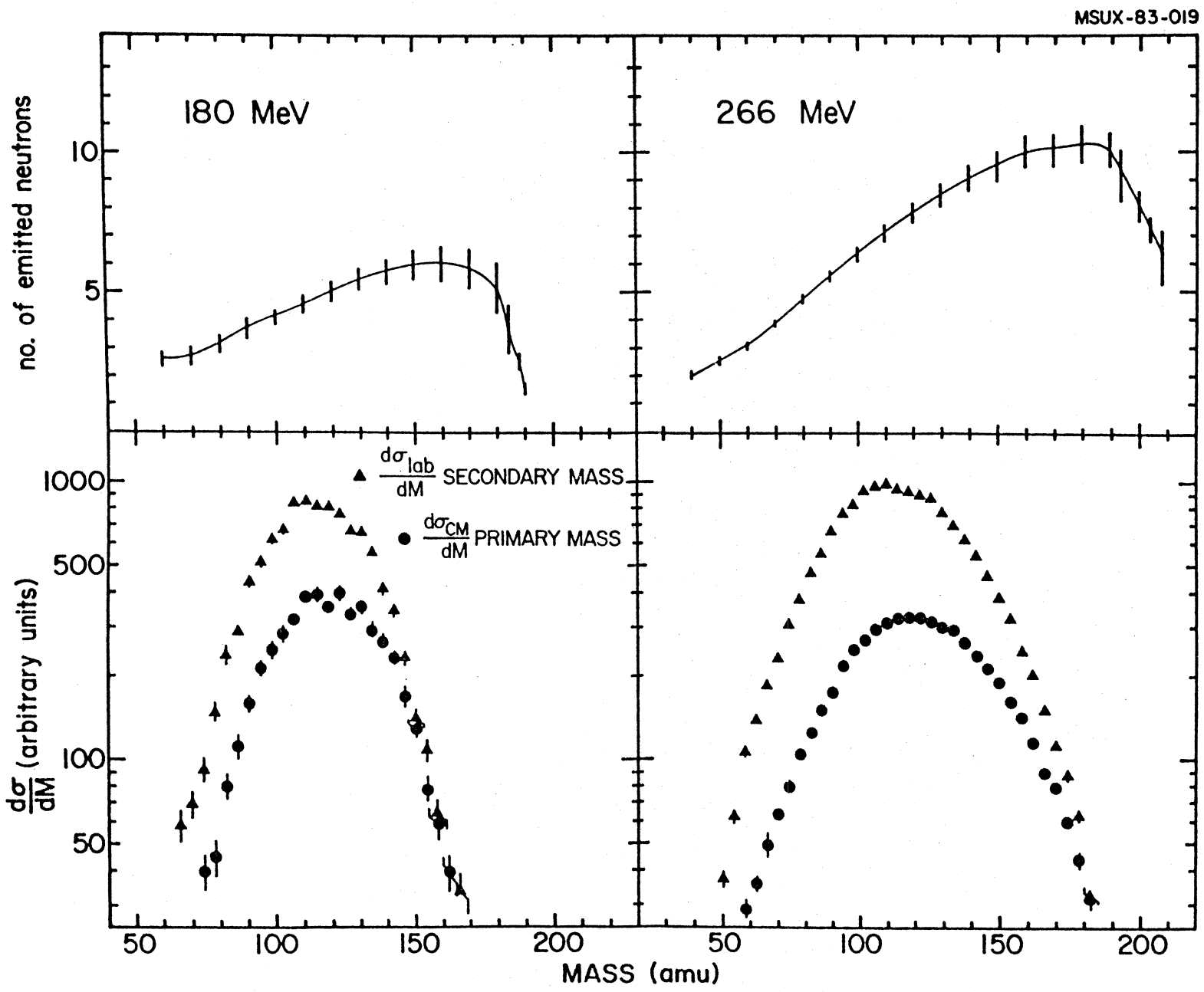
MSUX-83-019
180 MeV
266 MeV
no. of emitted neutrons
10
5
1000
500
100
50
dσ/dM (arbitrary units)
dσ_lab/dM SECONDARY MASS
dσ_CM/dM PRIMARY MASS
50
100
150
200
MASS (amu)

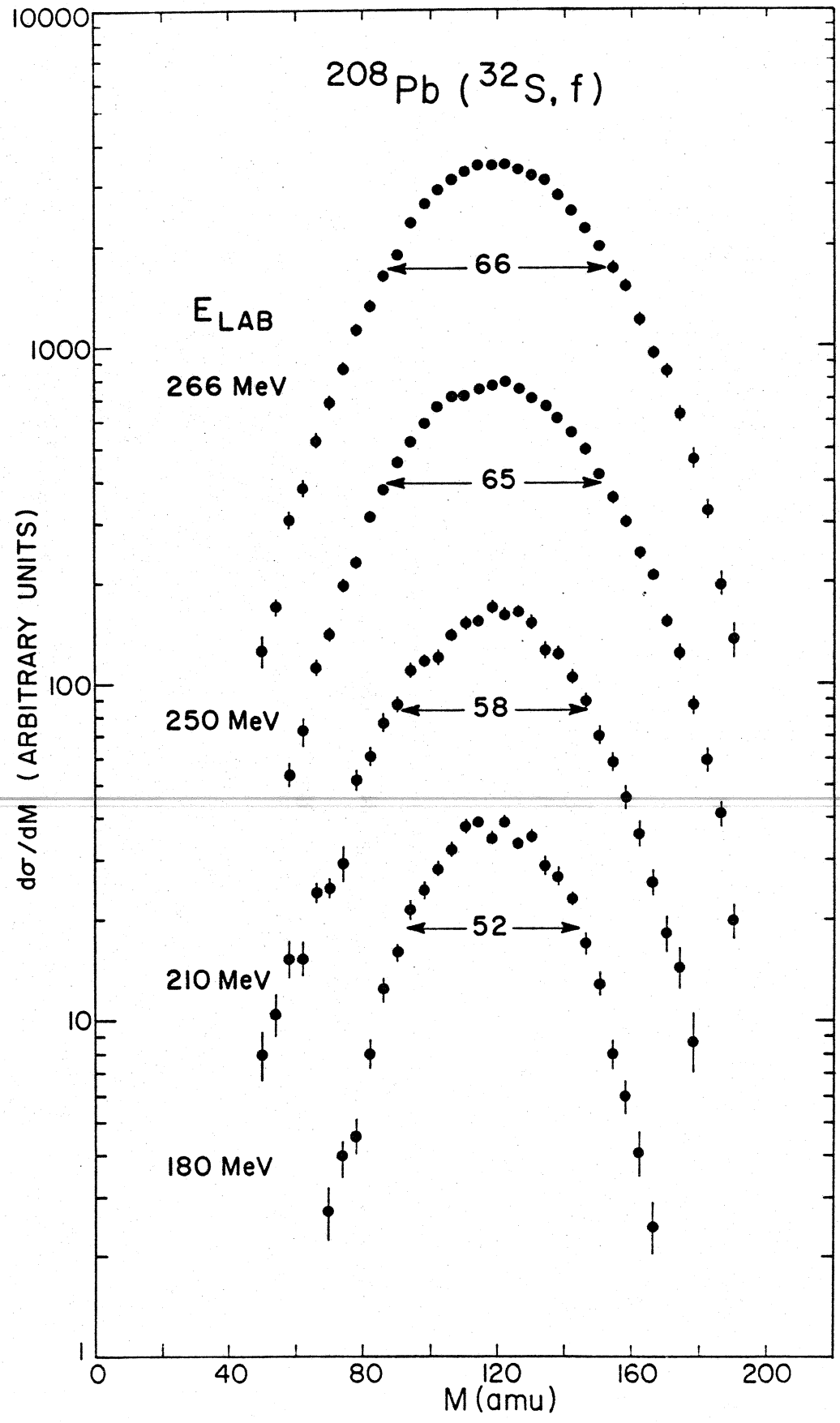
^{208}Pb (^{32}S, f)
E_{LAB}
266 MeV
250 MeV
210 MeV
180 MeV
66
65
58
52
10000
1000
100
10
1
0
40
80
120
160
200
M (amu)
dσ/dM (ARBITRARY UNITS)

Fig. 6

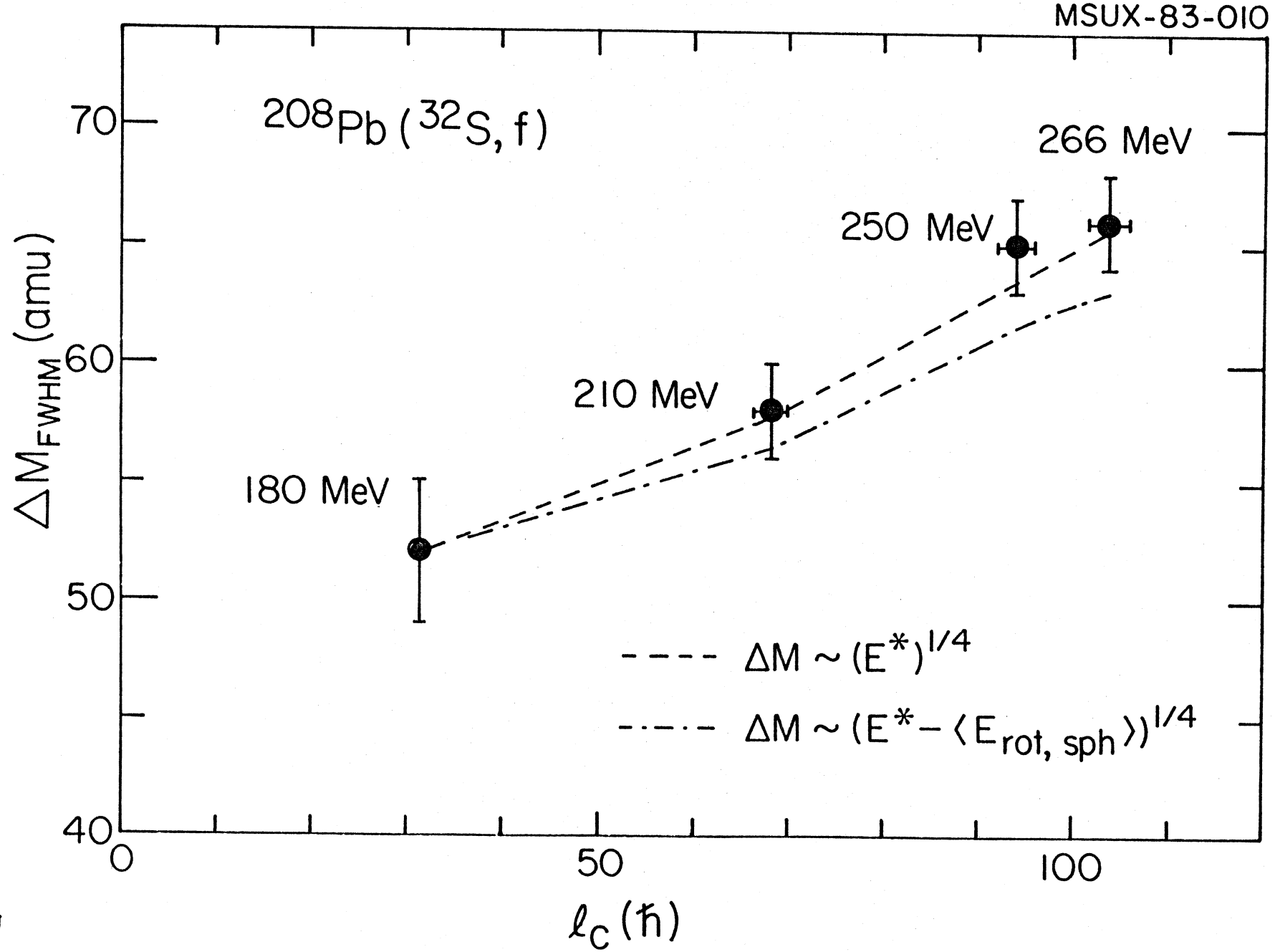
MSUX-83-010
^{208}Pb (^{32}S, f)
266 MeV
250 MeV
210 MeV
180 MeV
$\Delta M \sim (E^*)^{1/4}$
$\Delta M \sim (E^* - \langle E_{rot,\,sph} \rangle)^{1/4}$
ΔM_{FWHM} (amu)
70
60
50
40
0
50
100
ℓ_c ($\hbar$)

Fig. 7

MSUX-83-003

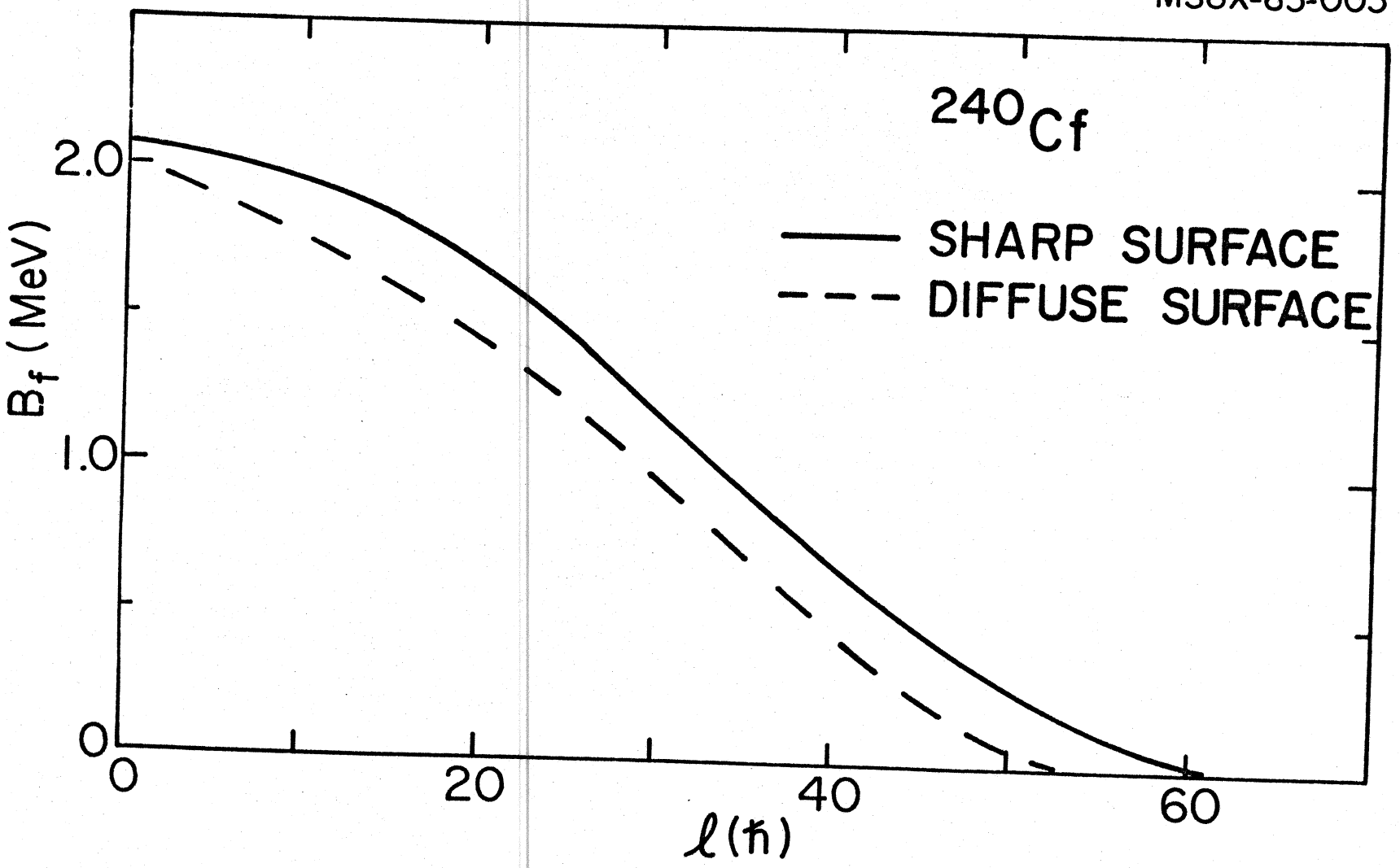

Fig. 8

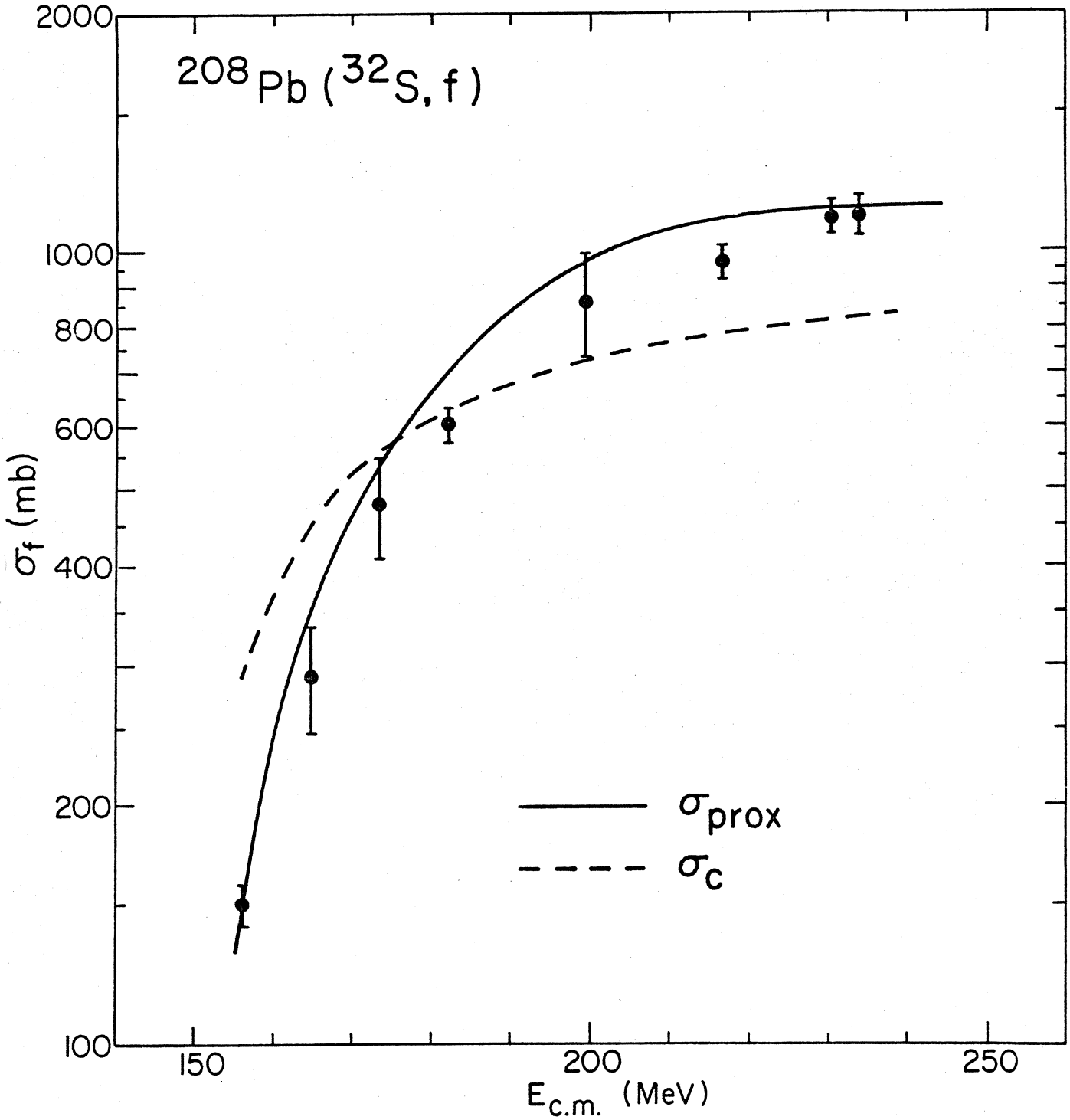
$^{208}Pb(^{32}S, f)$
σ_f (mb)
2000
1000
800
600
400
200
100
150
200
250
$E_{c.m.}$ (MeV)
σ_{prox}
σ_c

Fig. 9

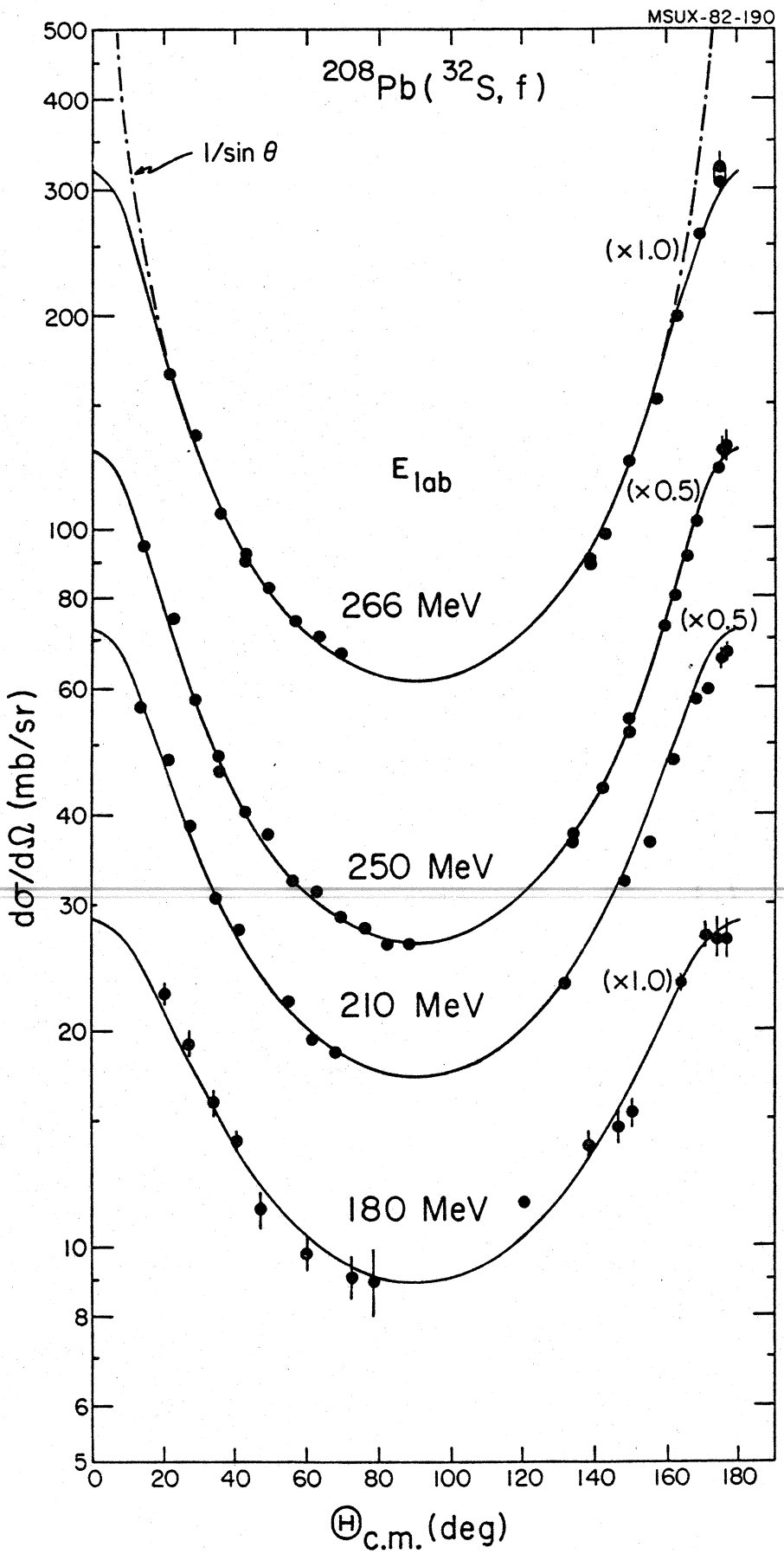
MSUX-82-190
$^{208}Pb(^{32}S, f)$
1/sin θ
E_{lab}
266 MeV
250 MeV
210 MeV
180 MeV
(×1.0)
(×0.5)
(×0.5)
(×1.0)
dσ/dΩ (mb/sr)
Θc.m. (deg)
500
400
300
200
100
80
60
40
30
20
10
8
6
5
0
20
40
60
80
100
120
140
160
180

Fig. 10

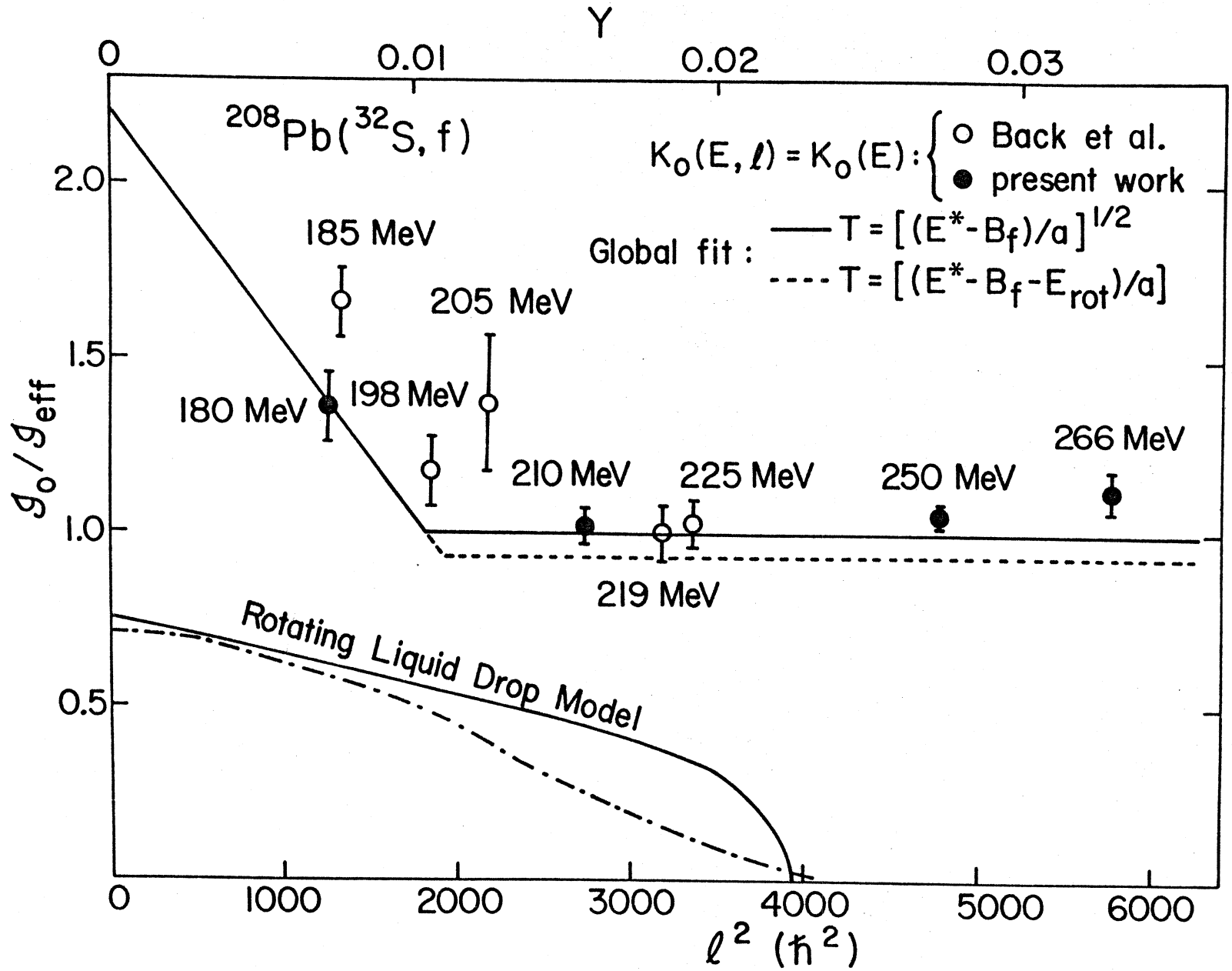
Y
0
0.01
0.02
0.03
$^{208}Pb(^{32}S, f)$
$K_0(E, \ell) = K_0(E)$:
Back et al.
present work
Global fit :
$T = [(E^* - B_f)/a]^{1/2}$
$T = [(E^* - B_f - E_{rot})/a]$
185 MeV
205 MeV
180 MeV
198 MeV
210 MeV
225 MeV
250 MeV
266 MeV
219 MeV
Rotating Liquid Drop Model
g_0/g_{eff}
2.0
1.5
1.0
0.5
0
1000
2000
3000
4000
5000
6000
ℓ^2 ($\hbar^2$)

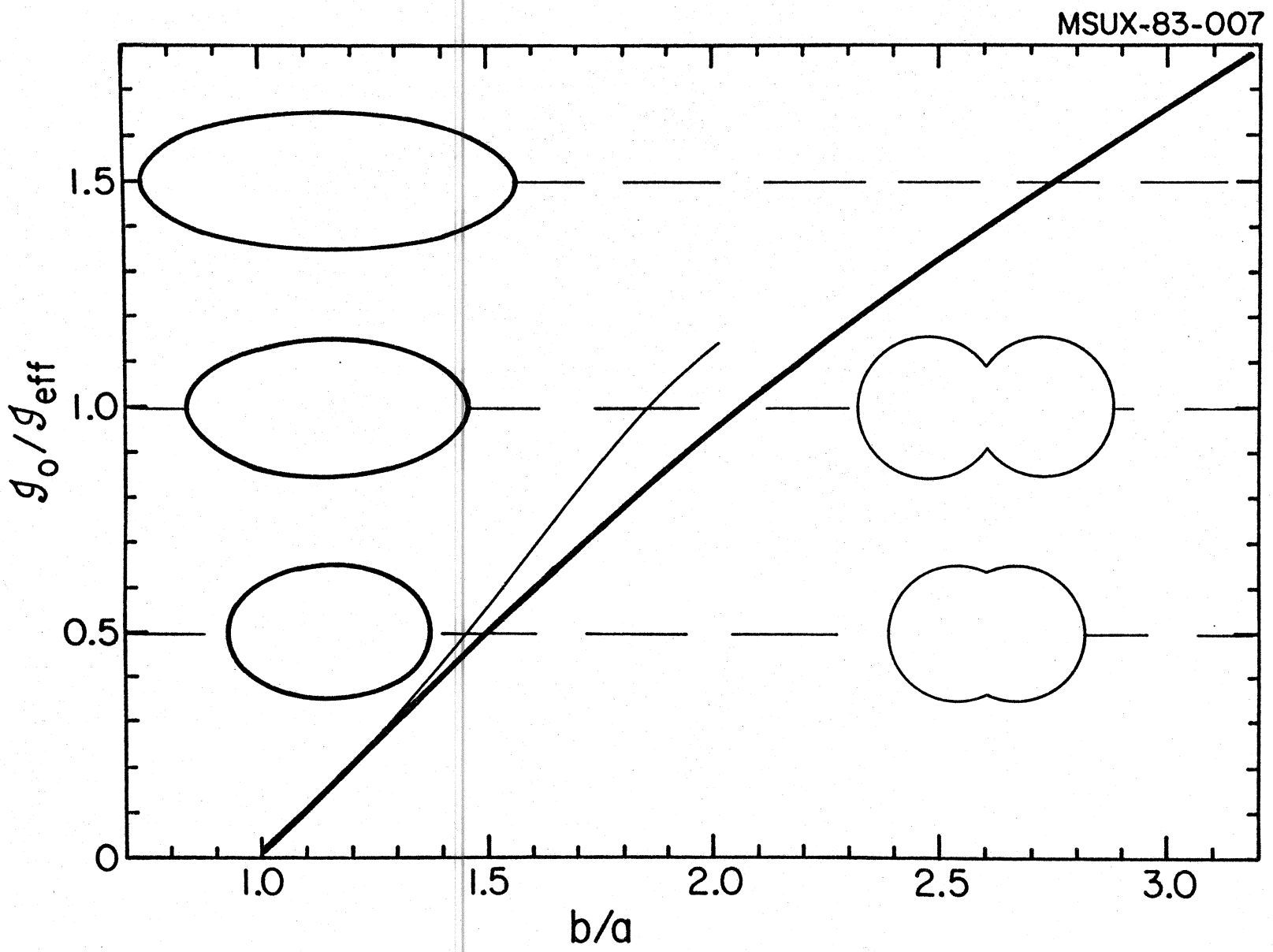

Fig. 12

MSUX-83-002

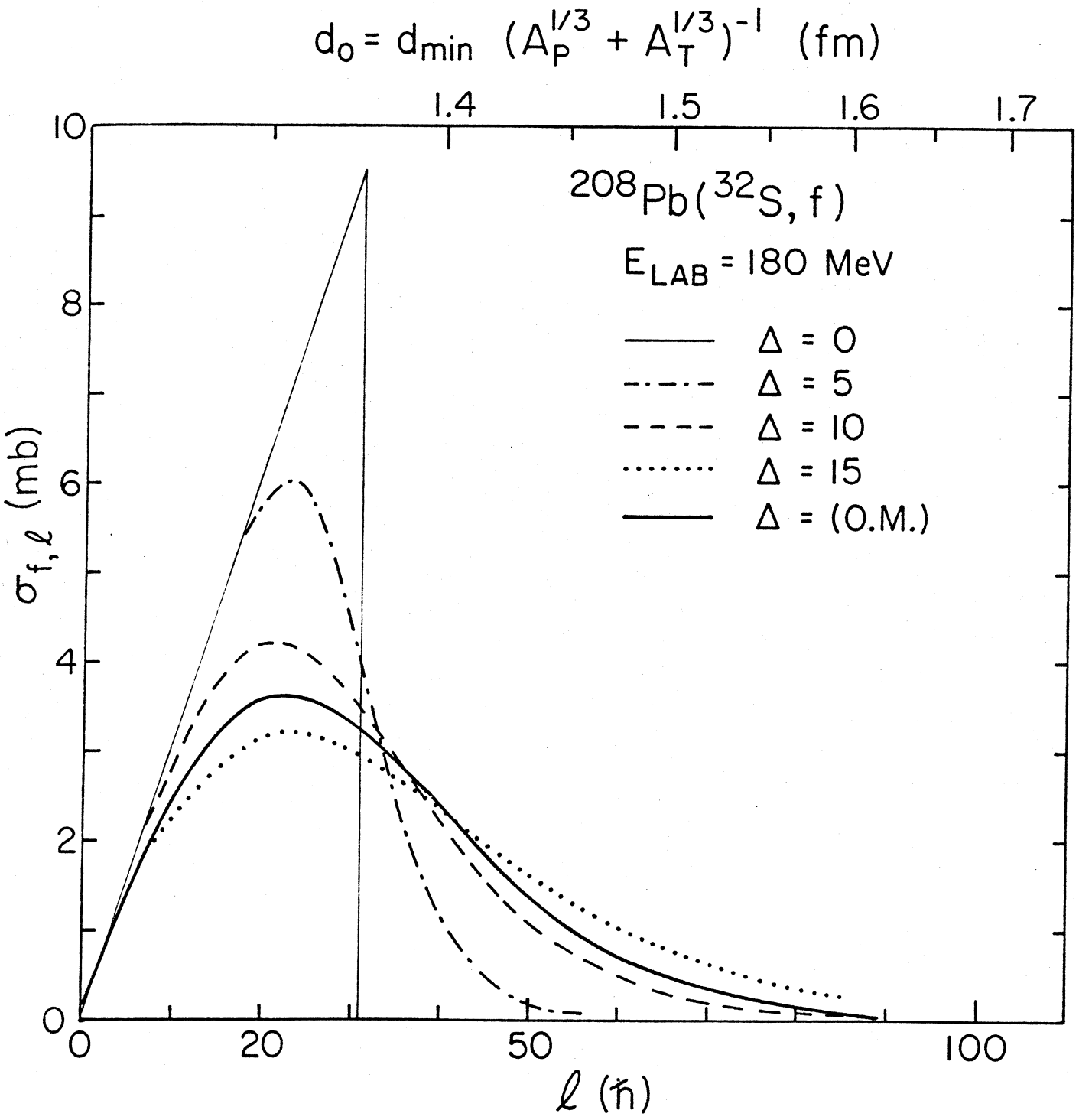

Fig. 13

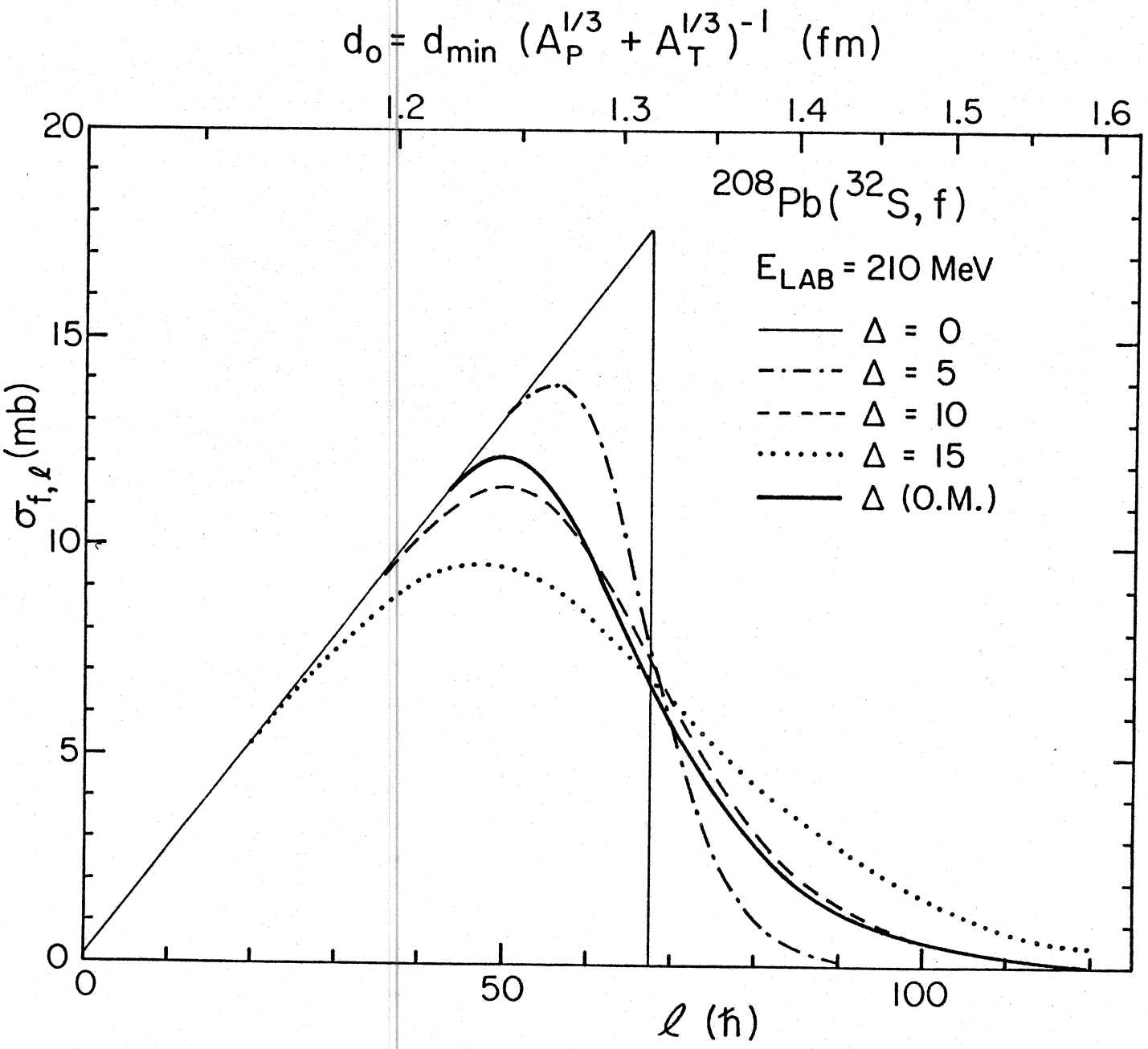
$d_o = d_{min}\ (A_P^{1/3} + A_T^{1/3})^{-1}$ (fm)
1.2
1.3
1.4
1.5
1.6
20
15
10
5
0
^{208}Pb(^{32}S, f)
E_{LAB} = 210 MeV
Δ = 0
Δ = 5
Δ = 10
Δ = 15
Δ (O.M.)
$\sigma_{f,\ell}$ (mb)
0
50
100
ℓ (ħ)

Fig. 14

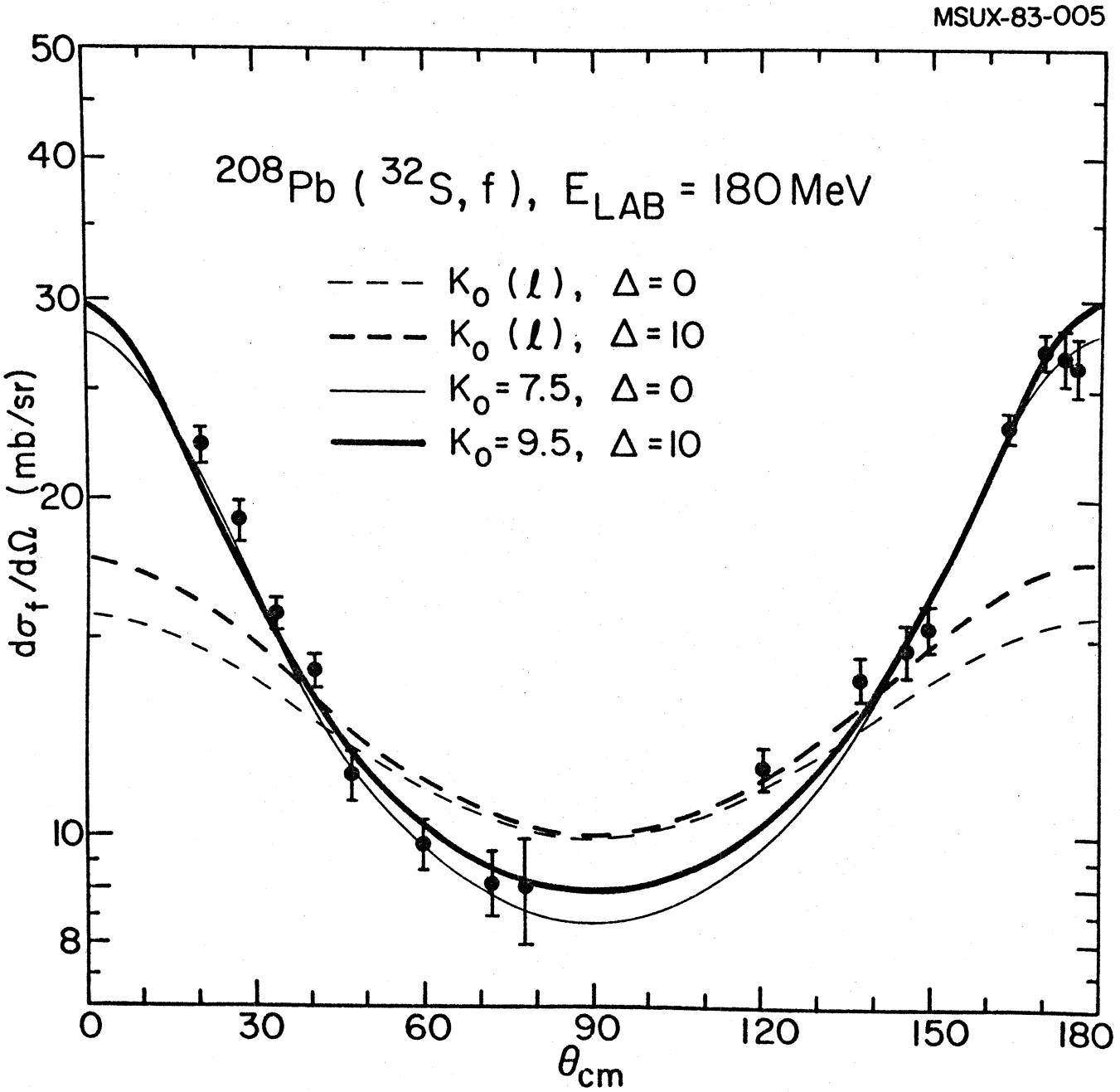
MSUX-83-005
^{208}Pb (^{32}S, f), E_{LAB} = 180 MeV
K_0 (ℓ), Δ = 0
K_0 (ℓ), Δ = 10
K_0 = 7.5, Δ = 0
K_0 = 9.5, Δ = 10
$d\sigma_f/d\Omega$ (mb/sr)
θ_{cm}
50
40
30
20
10
8
0
30
60
90
120
150
180

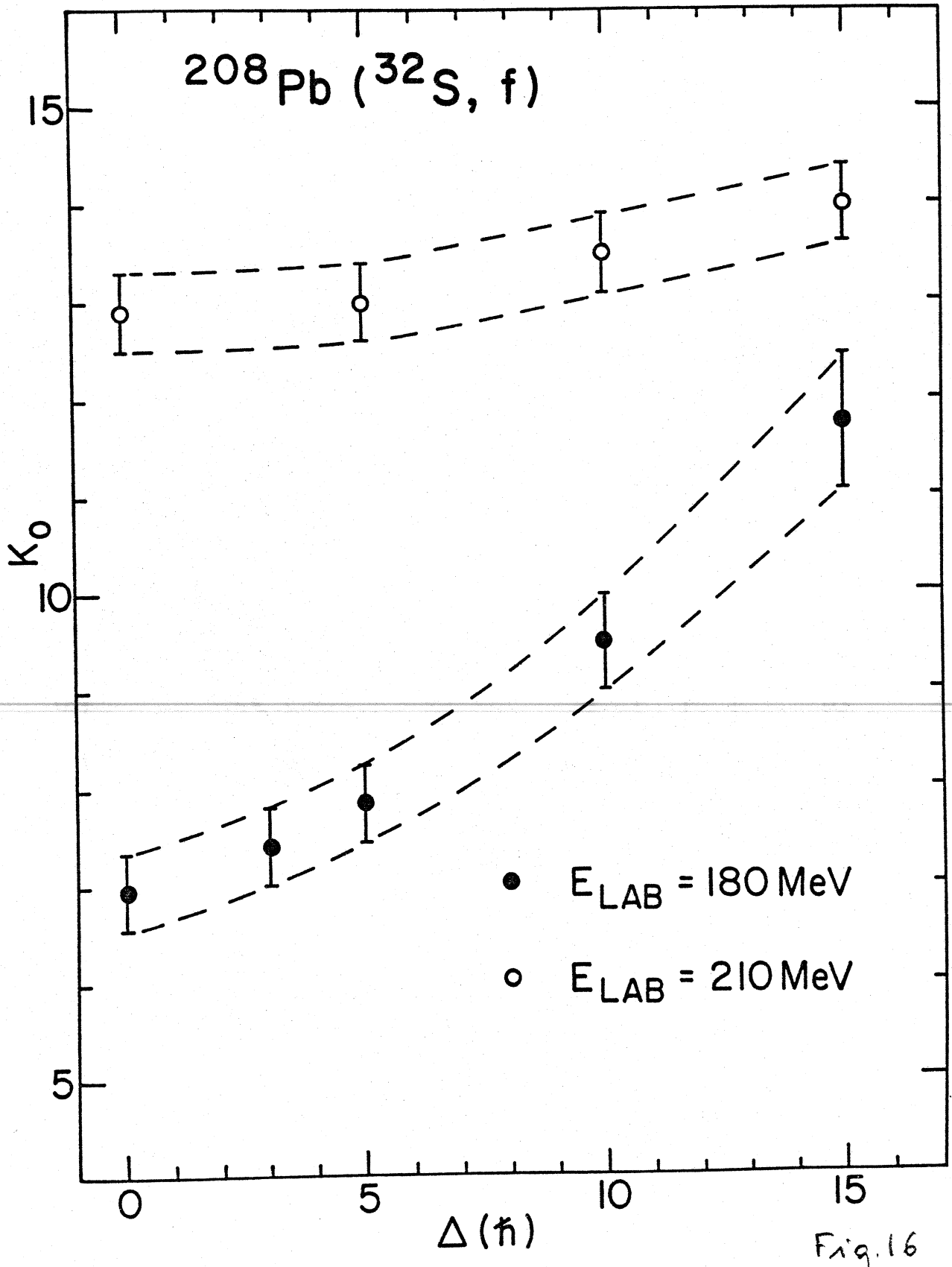
^{208}Pb (^{32}S, f)
15
10
5
K_0
0
5
10
15
Δ ($\hbar$)
E_{LAB} = 180 MeV
E_{LAB} = 210 MeV

Fig. 16

MSUX-83-006

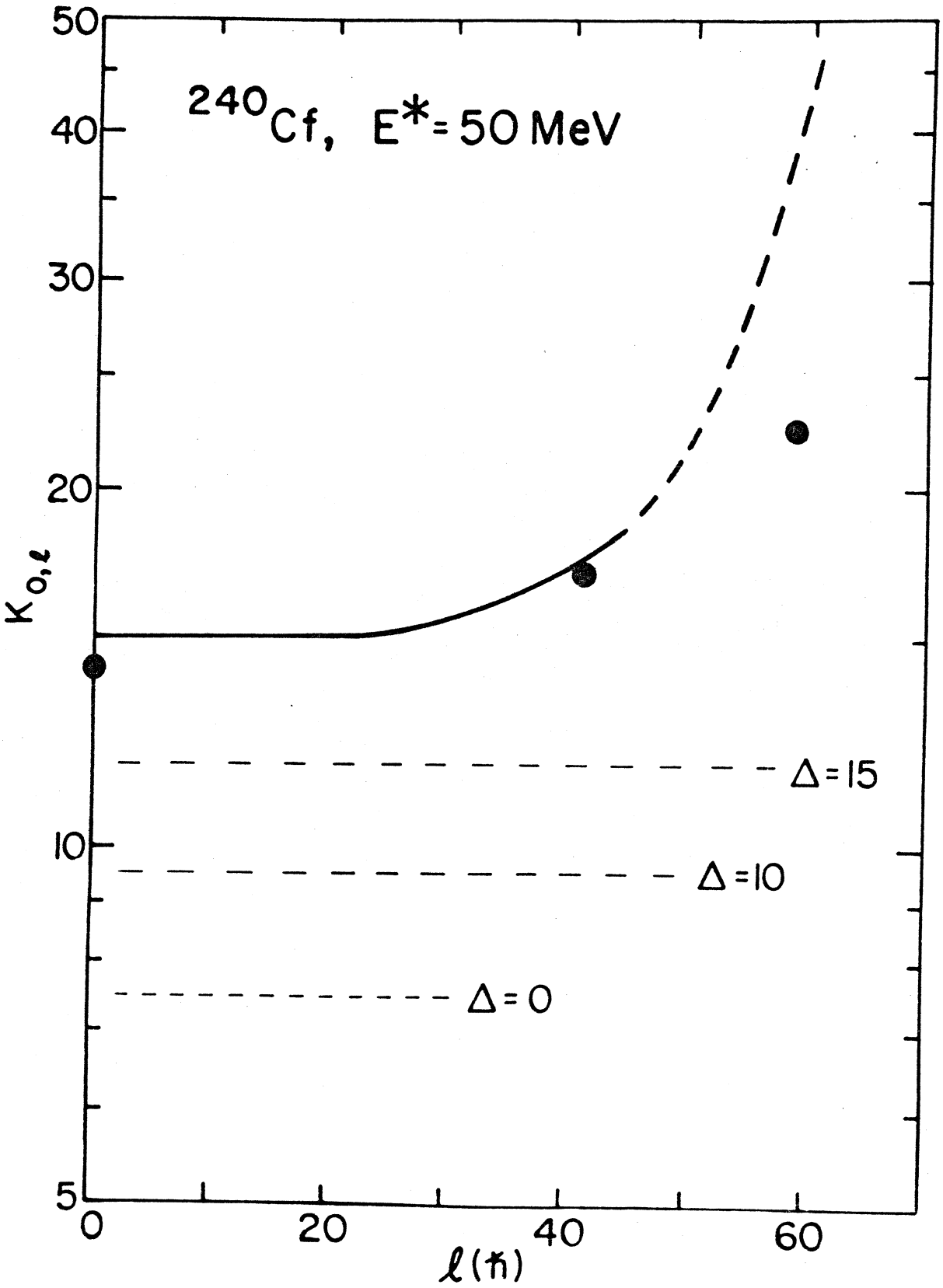

Fig. 17